PROPELLER INSTALLATION EFFECTS ON TURBOPROP ACOUSTICS

Giulia Chirico[a], George N. Barakos[a,*], Nicholas Bown[b]

[a] *CFD Laboratory, School of Engineering, University of Glasgow, G12 8QQ, UK*
[b] *Dowty Propellers, Anson Business Park, Cheltenham Road East, Gloucester, GL2 9QN, UK*

Abstract

Propeller installation options for a twin-engined turboprop aircraft are evaluated at cruise conditions, aiming to identify the quieter configuration. Computational fluid dynamics is used to investigate the near-field acoustics and transfer functions are employed to estimate the interior cabin noise. Co-rotating and counter-rotating installation options are compared. The effect of propeller synchrophasing is also considered. The employed method captures the complexity of the acoustic field generated by the interactions of the propeller sound fields among each other and with the airframe, showing also the importance of simulating the whole problem to predict the actual noise on a flying aircraft. Marked differences among the various layouts are observed. The counter-rotating top-in option appears the best in terms of acoustics, the top-out propeller rotation leading to louder noise because of inflow conditions and the occurrence of constructive acoustic interferences. Synchrophasing is shown to be beneficial for co-rotating propellers, specially regarding the interior noise, because of favorable effects in the interaction between the propeller direct sound field and the noise due to the airframe. An angle closer to the maximum relative blade shift was found to be the best choice, yielding, however, higher sound levels than those provided by the counter-rotating top-in layout.

*Corresponding author
Email addresses: g.chirico.1@research.gla.ac.uk (Giulia Chirico), George.Barakos@glasgow.ac.uk (George N. Barakos), Nicholas.Bown@dowty.com (Nicholas Bown)

Keywords: turboprops noise, CFD, propellers installation, synchrophasing

NOMENCLATURE

Acronyms

BPF Blade Passing Frequency

CFD Computation Fluid Dynamics

CO Co-rotating propellers

CNTI Counter-rotating top-in propellers

CNTO Counter-rotating top-out propellers

OSPL Overall Sound Pressure Level

SPL Sound Pressure Level

TF Transfer Function

Latin

Frequency	f [Hz]
Pressure coefficient	$C_p = \frac{p}{\frac{1}{2}\rho_\infty V_\infty^2}$ [-]
Longitudinal coordinate	X [m]
Propeller radius	R [m]
Unsteady pressure field	$p'(\mathbf{x}, t)$ [Pa]

Greek

Azimuthal position of the reference blade	ψ_b [deg]
Blade azimuthal coordinate	ψ [deg]
Fuselage azimuthal coordinate	Θ [deg]
Starboard propeller synchrophase angle	ψ_s [deg]

1. Introduction

Short to medium range flights make up to 95% of the total air traffic on European routes. Propeller-driven aircraft are the best option to decrease the fuel burnt during these flights, as they have a considerably higher propulsive

efficiency in comparison to a similar capacity jet aircraft. However, future environmental certifications will also require a cut in the aircraft acoustic emissions: compared to the capabilities of typical new aircraft in 2000, European targets aim to reduce the perceived acoustic footprint of flying aircraft by 50% for 2020[1] and to achieve a total noise abatement of 65% for 2050[2]. Current turboprops still emit substantial noise (on average, the interior noise is around 25 dB higher than a turbofan aircraft) and, because of the several tone components forming the propeller sound spectra, they are also perceived by passengers as more annoying than turbofan. Therefore, the challenge is to improve propeller acoustics without a significant performance penalty.

Starting from the IMPACTA project[3, 4] of Dowty Propellers, which aimed to reduce and/or modify the noise spectra of the whole turboprop propulsion system, this work analyses the near-field acoustics that is generated by different propeller installations. Computational Fluid Dynamic (CFD) is used to study a complete twin-engined turboprop aircraft, in particular evaluating the fuselage exterior noise, as well as the interior cabin sound levels via experimentally obtained transfer functions. Co-rotating propellers and counter-rotating configurations with top-in and top-out rotating propellers, the last one having proven more aerodynamically efficient[5], are considered. The main advantages of counter-rotating propellers are the natural balance of roll and yaw moments and of the P-factor, hence no engine is critical in this layout[6]. For these reasons, they are sometimes employed on military aircraft, of which a recent and peculiar example is the A400M military transport aircraft. This four-engine, eight-bladed, turboprop aircraft uses adjacent pairs of counter-rotating propellers to maximize efficiency[7], while the high internal noise has to be managed by passive and active noise control methods[7, 8]. Civil turboprops adopt, instead, co-rotating propellers (see Table 1) because of their lower maintenance costs and logistic reasons, since only one type of spare engine/gearbox and blades have to be carried by requirement. The two propellers are always assumed to be synchronized, i.e. their RPM precisely match, as it is usually done to improve passenger and crew comfort, since an audible vibration arises if the

Aircraft	Category	Layout	Synch.
Bombardier Dash8 Q400	Civil	Co-rot.	YES
ATR 72	Civil	Co-rot.	YES
Fokker F50	Civil	Co-rot.	YES
Saab 2000	Civil	Co-rot.	YES
Fairchild-Dornier 328	Civil	Co-rot.	YES
Piper PA-44 Seminole	Civil	Counter-rot.	YES
Lockheed C-130J Super Hercules	Military	Co-rot.	YES
Lockheed P-3 Orion	Military	Co-rot.	YES
Alenia C-27J Spartan	Military	Co-rot.	YES
Airbus A400M Atlas	Military	Counter-rot.*	YES
Bell Boeing V-22 Osprey	Military	Counter-rot.	NO

Table 1: Configuration of the main turboprop, with tractor propellers, and tilt-rotor aircraft currently operating, or of the recent past. * on each wing.

propellers do not turn at the same angular velocity. The two propellers are also considered in phase in the first part of the work, where co- and counter-rotating layouts are compared. The acoustic effect of synchrophasing, i.e. a relatively fixed shift in the propellers blades position, is then investigated for the usually adopted co-rotating layout as it had previously proven effective in reducing both vibration and noise levels[9–13]. Synchrophasing is a very interesting passive noise-control strategy because it does not require additional aircraft weight in its implementation. The idea is to set a specific phase angle between the propellers so that the acoustic interference among the different sound sources promotes noise cancellation. Since constant-speed variable-pitch propellers are typically employed, the desired propeller relative blade angle is simply attained by accelerating or decelerating the slave propeller via small adjustments in the blade pitch.

It is emphasized that the goal of the present research is not to estimate the abso-

lute noise levels of each propeller installation layout, but to carry out a relative study to find if one configuration is acoustically advantageous with respect to others.

Installed propellers were initially studied in the eighties and nineties when high oil prices made them an attractive alternative to the wider employed turbojets. Major efforts were carried out in the USA and Europe via experiments and numerical calculations. The aerodynamics and acoustics of the problem were investigated, both being linked to the aircraft sale and cost of use. Table 2 presents a summary of major works related to propellers installed on aircraft with tractor propeller configuration. Relevant findings of this research are: *(i)* the mutual interaction propeller-airframe is significant for both and unsteady, thus steady actuator disk computations can only give an average field estimate while time marching 3D simulations are needed to accurately capture interaction phenomena, especially in the case of propeller operating at incidence[24–28]; *(ii)* fuselage scattering, wing and nacelle reflections and boundary layer refraction must be included for adequate sound levels predictions, hence direct noise computations are "viable and reliable" in the near-field provided an appropriate mesh density, since they naturally account for these non-linear propagation effects[23]; *(iii)* the cabin noise is mainly due to the first three propeller tones[35] and, in the case of co-rotating propellers, it is dominated by the propeller approaching the fuselage when moving upwards, both in the forward and the rear fuselage parts[34]. Nowadays, because of environmental issues, interest in propeller-driven aircraft returned and new research is developing again, focusing especially on propeller acoustics. Exploiting the capabilities of modern computers, CFD techniques are often employed to study the near-field propeller noise. Work on isolated propellers is performed with the objective of strengthening an accurate noise prediction methodology with reasonable computational cost (see [37, 38] amongst others) or to find a quieter propeller design (see e.g. [39, 40]). Investigations on installed propeller configurations seek to improve our understanding of the complex propeller-airframe interaction phenomena and to find

Project and Sponsor	Experimental Activities	Numerical Activities
PTA (NASA)	Full-scale in-flight campaign[14, 15] using the SR-7L advance propeller[16, 17]: acoustic measurements, near and far from the propeller, to map the noise source directivity pattern under a wide set of operating conditions (altitude, propeller tip speed and prop-fan inflow angle varying).	• Noise predictions based on Farassat's formulations of the FWH equation, without the quadrupole term[18, 19], including fuselage scattering and refraction[20], using aerodynamics and aeroelasticity as input. • Near-field noise estimates with frequency domain methods[21, 22] vs direct evaluation using 3D unsteady Euler computations[23].
GEMINI II (European Commission)	Wind tunnel experiments of full-span model scaled of typical 50-seater commercial twin-engined turboprop[24] to investigate the aerodynamic interactions between propeller slipstream and airframe at transonic conditions.	Euler/Navier-Stokes computations (time accurate vs steady state adopting an actuator disk method to represent the propeller)[25, 26].
APIAN (European Commission)	Wind tunnel tests campaign for the enhanced GEMINI II model[27]: aerodynamic and acoustic measurements.	Steady and unsteady Euler simulations combined with the ONERA radiation acoustic code, solving the FWH equation in the frequency domain, and the NLR acoustic code for scattering and refraction [28].

Table 2: Main efforts performed in the past to study aerodynamics and acoustics of installed propellers (Part 1). FWH stands for Ffowcs Williams - Hawkings.

Project and Sponsor	Experimental Activities	Numerical Activities
research activities (FFA)	Low-speed wind tunnel survey on a propeller-nacelle-wing scaled model[29, 30] varying incidence, yaw, free-stream speed, propeller thrust coefficient and nacelle geometry: surface pressure and propeller slipstream flow-field data acquired; no acoustic measurements made.	• Time-averaged panel code predictions, coupled with a propeller slipstream model employing momentum-blade element theory[31, 32]. • Unsteady Euler and Navier-Stokes simulations with the DLR TAU code[33].
SAAB industrial activities (FAA and SAAB)	• In-flight acoustic measurements of interior and exterior noise of the twin-engined, co-rotating, turboprop SAAB 2000[34]. • Thorough study of both tonal and broadband noise sources on the aircraft, together with passive and active tailored control measures adopted[35].	Calculations with a time-domain linearized version of the FWH equation[36] including non-uniform propeller inflow and time-varying blade loads[34].

Table 2: Main efforts performed in the past to study aerodynamics and acoustics of installed propellers (Part 2). FWH stands for Ffowcs Williams - Hawkings.

acoustically better installation solutions, as for example in [41] or in the German BNF project[42, 43] for a tractor configuration and in the European CESAR project[44, 45] for a pusher configuration.

Whereas the above cited works analyze a propeller-engine-wing combination, this research considers the full turboprop aircraft, aiming to assess the influence of the propeller installation layout, i.e. co-rotating vs counter-rotating propellers, on the airplane acoustics. Numerical computations are performed using the compressible Unsteady Reynolds Averaged Navier-Stokes (URANS) equations which have been already proven successful in propeller near-field noise predictions and in similar research efforts on contra-rotating open rotors (e.g. [46–48]) and marine propellers (e.g. [49]).

Concerns about possible high sound levels developed by propellers operating at transonic or supersonic tip speeds designed in the 1980s drove, already at that time, studies on propeller synchrophasing as a means of noise reduction. Analytical and experimental attempts to study the problem, modelled using monopole/dipole sources and a cylindrical shell representing the fuselage, showed that the propeller phase angles do not significantly alter the external pressure field but affect considerably the internal one[11, 12]. The latter appears to be directly coupled with the cylinder vibration modes which govern the sound transmission and the propagation in the cabin interior. These investigations also indicated that the acoustic energy comes in and out of the fuselage in localized regions whose position strongly depends on the propeller phase shift, the majority of the energy entering in any case over a length of one shell diameter. An analytical technique to optimize the propeller phase angles, based on a systematic search among combinations of propellers signatures in the frequency domain, was presented in [9] and employed with the flight-test data of a NATC Navy/Lockheed P-3C. Results clearly showed that synchrophasing can vary the total sound energy, and not only redistribute it, yielding a reduction up to 8 dB of the average cabin noise in a four-engined aircraft and 1.5 dB in a twin-engined[9, 10]. All cited works underlined that the optimum synchrophase angle varies with cabin location, sound frequency and fuselage layout, thus the angle

selection is a compromise and configuration-dependent. Flight and environmental conditions have recently been proved to also influence the synchrophase optimum[50], showing that the synchrophaser should be ideally adaptive, and that this could be achieved with a small number of microphones if placed in the right locations. Investigations on adaptive synchrophasing controllers have been carried out by different organizations, resulting in tested prototypes and various patents such as [51–56]. Nevertheless, usually the synchrophase angles are set a priori into the electronic synchrophasing system and thus a preliminary optimization study becomes important to obtain noise reduction for the primary aircraft operating conditions. The analytical propeller signature analysis technique is still currently used for these studies[13, 57], using experimental data as input. It is, however, noted that this theory implies that the contributions of each propeller combine in a linear way, which seems a reasonable assumption from the comparison with experimental data but it is not well proven.

Instead, the use of CFD in this work enables to investigate the whole acoustic near-field that is generated using synchrophased propellers, analyzing the phenomenon and assessing the possible noise benefits of this strategy. Various propeller synchrophase angles are considered, and the different cases are compared regarding both exterior and interior sound levels.

2. Test Cases

The airplane considered in this study is a twin-engined turboprop, with a standard commercial high-wing design and a capacity of around 70-80 passengers, similar to the ATR72, the Bombardier Dash 8 series or the Fokker 50. The computational geometry of the aircraft is shown in Figure 2(b) along with its dimensions. It is an aircraft generic shape without horizontal and vertical tail surfaces adopted in the IMPACTA project[3, 4].

All the three propeller installation options, considering the two propellers in phase, are analyzed:

(a) Co-rotating propellers **(CO)**: conventional layout for civil aircraft with both

propellers rotating clockwise as viewed from the rear - see Figure 1(a);

(b) Counter-rotating top-in propellers **(CNTI)**: port propeller rotating clockwise and starboard propeller counterclockwise as viewed from the rear, thus both propellers approach the fuselage when moving downwards - see Figure 1(b);

(c) Counter-rotating top-out propellers **(CNTO)**: opposite of **CNTI**, port propeller rotating counterclockwise and starboard propeller clockwise as viewed from the rear, thus both propellers approach the fuselage when moving upwards - see Figure 1(c).

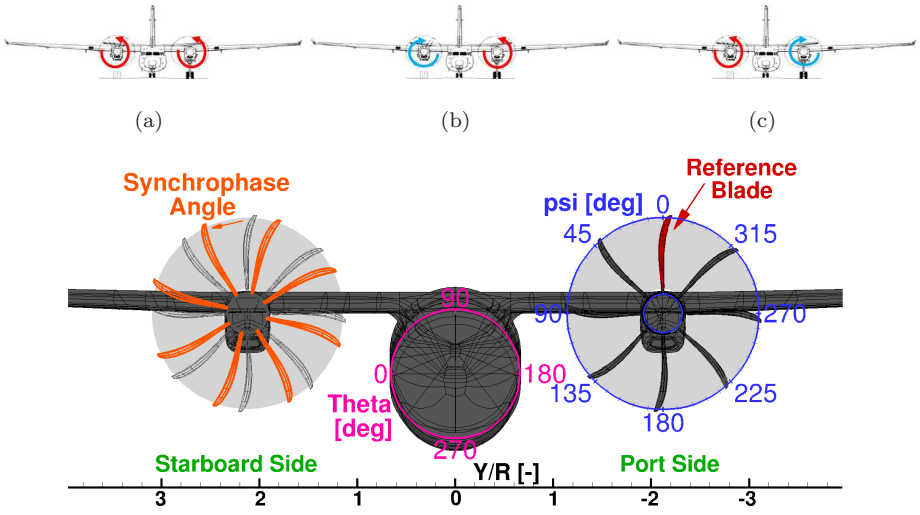

Figure 1: Definition of the turboprop layout and of the systems of reference used (frontal view). (a) **CO** - co-rotating, (b) **CNTI** - counter-rotating top-in, and (c) **CNTO** - counter-rotating top-out propellers installation options. (d) Definition of reference blade, blade azimuth angle ψ (increasing with the propeller rotation, regardless of the direction), fuselage azimuth angle θ and positive synchrophase angle ψ_s (shifted blades in orange).

For the synchrophasing study on the co-rotating layout, the port propeller is considered as master, and the starboard propeller blades lead those of the port propeller for a positive synchrophased angle (refer to Figure 1(d)). Typical synchrophasing angles for twin-engined turboprops are between 10 and 15 degrees.

Four synchrophasing angles are considered: $\psi_s = 5, 10, 15$ and 30 deg. It is noted that, the propeller having eight blades, the maximum possible propellers blade shift is equal to $\psi_s = 22.5$ deg, and that a larger angle is equivalent to a negative synchrophase angle, e.g. $\psi_s = 30$ deg $\equiv -15$ deg.

The Propeller. In this research, the IMPACTA Baseline propeller was employed[40, 58]. It is a eight bladed new-generation propeller, with extremely low activity factor and designed to operate at high blade loading conditions. The geometric and the cruise operating parameters of the IMPACTA propeller are summarized in Table 3.

Radius R	2.21 m	Free-stream Mach number M_∞	0.5
Root chord c	0.213 m	Thrust line incidence	-2 deg
Pitch angle (0.7R)	$\sim 51^\circ$	Helical Mach number (0.95R)	0.789
Angular velocity	$\sim$850 RPM	Tip Reynolds number Re_{TIP}	1.24e06
Required Thrust	7852 N	Altitude	7620 m

Table 3: IMPACTA Baseline propeller parameters and nominal cruise operating conditions.

It is noted that a cruise flight is here considered, being usually the longer segment of the aircraft route where propellers are the major noise source. However, results can differ in the case of different flight conditions.

Simulations Details. Simulations were performed solving the URANS equations, as the most efficient CFD method able to capture the propeller tonal noise, which is the main contribution to the overall interior noise; no attempt was made at this stage to study the broadband noise content. The $k-\omega$ SST turbulence model[59] was employed to close the equations. Computations were started for all cases from unperturbed free-stream flow conditions, accelerating gradually the propeller up to the cruise angular velocity in the first half of propeller revolution. A temporal resolution of 1 degree of propeller azimuth, i.e. 360 steps per propeller revolution, was chosen to guarantee smooth and fast

convergence at each time-step resolved in the simulation (the resulting Nyquist frequency allows to solve up to frequencies well above the third propeller tone). Using 17 computing nodes, each with two 2.1 GHz 18-core Intel Xeon E5-2695 series processors, one complete propeller revolution took 66 hours. Five full propeller revolutions were run before reaching an adequate convergence of the global flow-field in the region of interest for the analysis.

3. Numerical Methodology

3.1. The Flow Solver HMB3

Numerical simulations were performed using the in-house parallel CFD solver Helicopter Multi Block (HMB3)[60–62] of the University of Glasgow. HMB3 solves the 3D Navier-Stokes equations in dimensionless integral form using the Arbitrary Lagrangian Eulerian formulation for time-dependent domains with moving boundaries, discretised via a cell-centered finite volume approach on a curvilinear co-ordinate system. Convective fluxes are treated with Osher's upwind scheme[63] and the viscous stress tensor is approximated using the Boussinesq hypothesis[64] or an explicit algebraic Reynolds stress model[65]. Several turbulence models, of the URANS and hybrid LES/URANS families, are implemented in the solver. The MUSCL variable extrapolation method[66] is employed, in combination with the van Albada limiter[67], to provide second-order accuracy and avoid spurious oscillations across shock waves. The temporal integration is performed with an implicit dual-time method and the linear system is solved using the generalized conjugate gradient method with a BILU[68] factorization as a pre-conditioner. The Message Passing Interface MPI tool is used for the communication between the processors in parallel execution.

Solver Validation. HMB3[60, 61] has been validated for propeller flows, in both isolated and installed configurations, by comparison with experimental data from the unswept JORP propeller[69] and the IMPACTA wind tunnel tests campaign[70, 71]. Results are presented in [58] and [40], respectively. Overall, a good agreement is observable regarding both aerodynamics and acoustics,

showing that HMB3 allows to predict the flow around the propeller blades, the aerodynamic phenomena due to the propeller-airframe interaction and the dominant noise tones of the acoustic near-field with an adequate accuracy.

3.2. Computational Grids

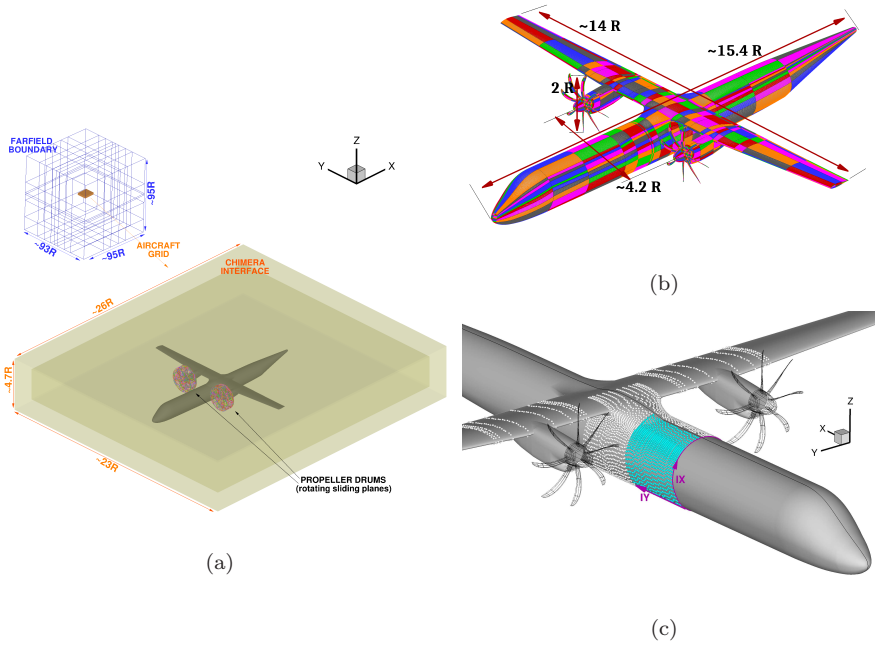

Figure 2: High-wing twin-engined turboprop aircraft: computational geometry and setup. Dimensions are reported as function of the propeller radius R. (a) Full grid layout visualization and system of reference definition. (b) Computational geometry with surface mesh visualization. (c) Numerical probes (in light-blue those used as input to the transfer functions in the interior noise estimation).

Multi-block structured grids, generated with the ICEM-Hexa^{TM} software of ANSYS, were employed. A fully-matched body-fitted mesh was built around the whole aircraft, adopting an "O" grid topology surrounding the surfaces of fuselage, wings and nacelles. Special attention was paid to have a good quality mesh in areas proved critical in preliminary tests, such as the fuselage-wing junction. Propellers are included in the airplane grid using the sliding plane

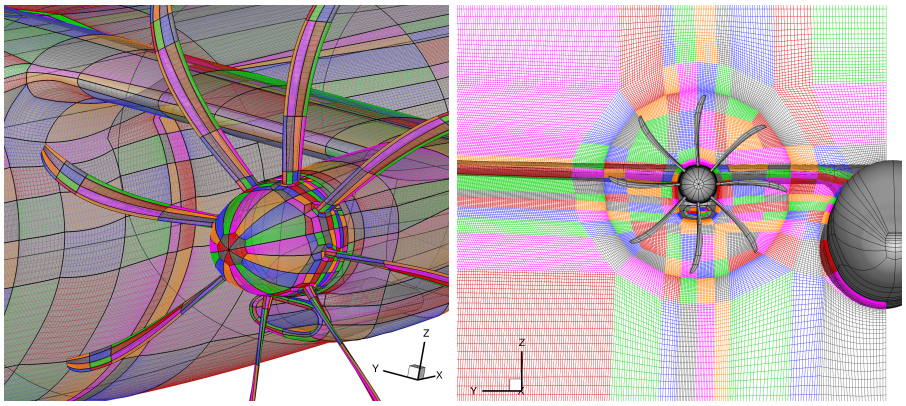

(a) (b)

Figure 3: High-wing twin-engined turboprop aircraft: computational grid visualizations. (a) Surface mesh detail: port propeller and inboard section of the wing. (a) Volume mesh: slice between the starboard propeller and the wing (frontal view).

technique[72] which allows the relative motion and the exchange of information between the two meshes with a set of pre-calculated interpolation weights. The grids for all different cases were thus obtained just selecting the appropriate propellers during the assembling process and simply applying a rotation of the starboard propeller drum by the desired synchrophased angle when necessary. The aircraft mesh is then immersed, with the chimera overset method[73], in a regular background grid which extends until the far-field. The layout of the complete grid, as well as block topology and mesh, are visualized in Figures 2 and 3. The aircraft grid was prepared for half of the model and then mirrored, thus to ensure perfect symmetry of the computational domain. Similarly, the propeller meshes were generated by copy-rotating a single-blade grid, mirroring in the case of opposite propeller rotation. Overall, the full grid counts 13326 blocks and 170 million cells, of which 132 million belong to the airplane mesh and 16.5 million to each propeller. The adopted spatial resolution guarantees, in the region of interest, a minimum of 17 points per wave length for the third propeller tone which was found adequate in previous solver validation studies.

Boundary Conditions. The aircraft surfaces are treated as solid walls. At the inlet boundaries, which are located far enough from the engine intakes, a surface pressure equal to the free-stream value is imposed and the other variables are extrapolated. Free-stream boundary conditions are applied on the external boundaries of the computational domain.

3.3. Noise Estimation Approach

Exterior Noise. The near-field noise is directly evaluated from the URANS solutions. Computing the unsteady pressure field $p'(\mathbf{x}, t)$ directly from the CFD results, the Overall Sound Pressure Level (OSPL) and the Sound Pressure Level (SPL) as function of the sound frequency are estimated as follows:

$$\begin{cases} \text{OSPL} = 10 \log_{10} \left(\frac{{p'_{rms}}^2}{{p_{ref}}^2} \right) \text{dB}, \\ \text{SPL}(f) = 10 \log_{10} \left(\frac{\text{PSD}(p')}{{p_{ref}}^2} \right) \text{dB}, \end{cases} \tag{1}$$

where *rms* stands for root mean square, PSD is the power spectral density and p_{ref} is the acoustic reference pressure which is equal to $2 \cdot 10^{-5}$ Pa.
Numerical probes are also included in the simulations to directly record the time pressure signal at some locations of interest. In particular, as shown in Figure 2(c), probes are located on the fuselage in the main propeller region of influence, from 1 R upstream to $\sim$ 1.6 R downstream the propeller plane, and along some span-wise wing stations and the engine intake.

Interior Noise. Within the activities of the IMPACTA project, NLR performed a series of tests on a Fokker 50 aircraft to determine the cabin noise response of a typical commercial airplane[74]. The sound transmission through the fuselage walls is shown to be non uniform in space and highly dependent on the frequency of the incoming pressure field, yielding noise reductions of more than 20 dB. The outcome of these experiments was a set of Transfer Function (TF) describing the relation existing between the external pressure field on the fuselage and the sound pressure inside the cabin. In this way, the aircraft structural response is accounted for without the need of a computational expensive structural model.

A stronger coupling between aeroacoustics and structural vibrations is beyond the scope of the analysis at this stage, since there is no intention to estimate absolute noise levels but only a relative comparison between the different configurations is of interest.

Data is available for a passenger located on the starboard side of the airplane, slightly ahead of the propeller rotational plane on the second seat from the window. The TF account for the sound pressure impinging on the fuselage region between 1 R upstream and ∼0.35 R downstream the propeller rotational plane (see Figure 2(c)) and cover a frequency range from $\frac{\mathrm{BPF}}{2}$ to over 10 BPF which is more than adequate for the study. Knowing the TF, the interior noise is simply estimated from their convolution with the exterior pressure signals computed by the CFD simulations. In particular, data recorded from the numerical probes for the last full propeller revolution run are used for this analysis. Reference [40] details the TF determination, their characteristics and their application.

4. Discussion of the Results

In the following, the aerodynamic and the acoustic fields of co- and counter-rotating configurations, with propellers in phase, are first investigated and compared. The acoustic analysis of the effects of propeller synchrophasing is after presented. For convenience, a cylindrical system of reference is introduced to present data on the aircraft fuselage: the fuselage azimuthal coordinate θ goes clockwise as viewed from the front of the aircraft as defined in Figure 1(d), and the longitudinal axis X is parallel to the fuselage centerline, positive in the flow direction and with its origin at the propeller rotational plane.

4.1. Co-rotating vs Counter-rotating Layouts.

4.1.1. Aerodynamic Analysis

To show the complex characteristics of the flow-field generated from the interaction of the tractor propellers with the airframe, in Figure 4 the vortical structures are shown for the co-rotating layout. The adopted mesh resolution

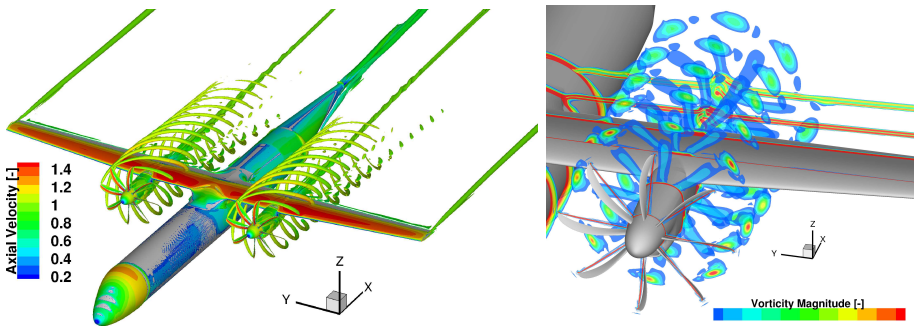

(a) (b)

Figure 4: Instantaneous vortical structures - **CO**, $\psi_b = 90$ deg. (a) Iso-surfaces of Q, colored by non dimensional axial velocity. (b) Vorticity contours for the port propeller.

preserves the propellers wake up to the aircraft tail. The interaction of the blade tip vortices with the wing is well captured by the CFD simulation which is able to show the different flow features of the flow-field in the case of top-in and top-out rotating propellers. The vortices generated from the wing tips, the nacelles and the inclination of the aft fuselage are also visible.

Aircraft Trimming Discussion. Because of the lack of the horizontal and vertical tail surfaces in the computational geometry, it was not expected to achieve a complete trim in the flight direction. A small thrust surplus with respect to the aircraft drag was in effect found for the nominal conditions simulated (see Table 3). However, mean wing and propeller loads are suitably representative of cruise conditions and, being primarily interested in a comparative study among the different installation layouts, no attempt to trim the aircraft by changing the blade pitch was carried out. A discrepancy of less than 0.03% in the total propellers thrust was registered between all cases analyzed and this was considered enough to achieve relative data with satisfactory accuracy. Regarding the aircraft trim state, the co-rotating configuration results in unbalanced forces and moments, and thus likely to get considerably more trim drag. This is not the case for the counter-rotating layouts because of their symmetry. The resulting side force Fy and roll moment Mx, scaled with the port propeller thrust

T_p and torque Q_p, respectively, are reported in Table 4 to quantify the natural aircraft equilibrium state, i.e. without any control surfaces.

	CO	**CNTI**	**CNTO**
Fy/T_p	21.303	0.046	0.001
Mx/Q_p	89.195	0.0215	0.0003

Table 4: Aircraft equilibrium state for the different installation layouts with no control surfaces active. Fy is the resultant side force, Mx the resultant roll moment, T_p and Q_p the thrust and torque of the port propeller.

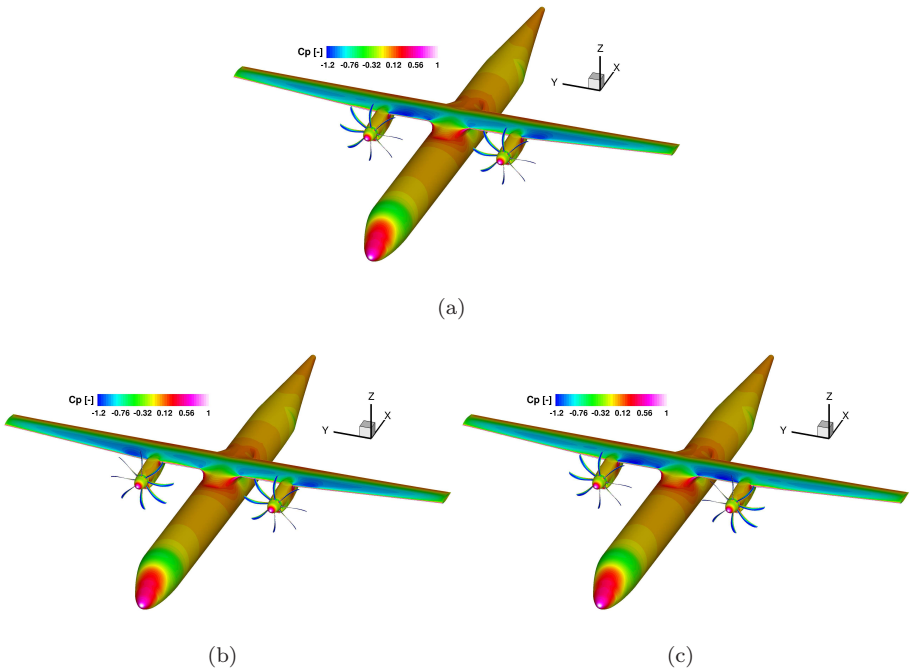

(a)

(b) (c)

Figure 5: Averaged pressure loading on the aircraft. (a) **CO**. (b) **CNTI**. (c) **CNTO**.

Aircraft Loads Analysis. Figure 5 shows the average surface pressure distribution on the aircraft for the various configurations. The influence of the propeller on the wing loading is visible, resulting in a different pressure distribution on the wing portion affected by the propeller slipstream depending on the propeller

rotation. In particular, the wing experiences higher loading on the propeller upwash side and, in the case of propeller top-out rotation, the suction area on the wing inboard upper surface is observed to extend up to the wing-fuselage junction. The pressure field is, as expected, symmetric in the case of counter-rotating layouts. A comparison of the average span-wise normal pressure loading of the

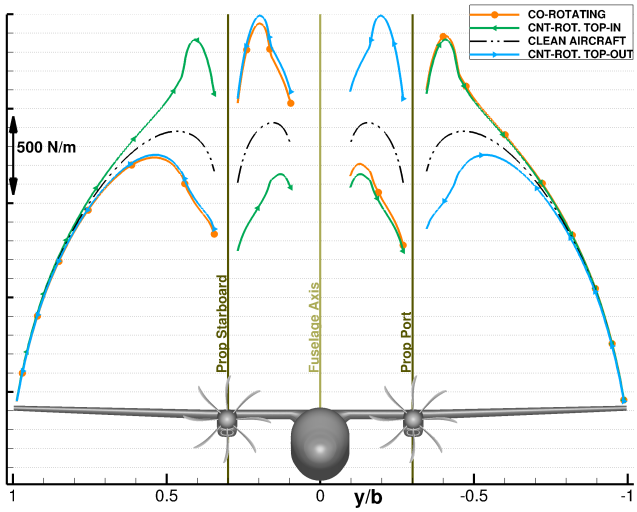

Figure 6: Span-wise normal averaged pressure force distribution over the wing: comparison between different layouts and clean aircraft as reference.

different configurations is presented in Figure 6. The lift gain and reduction due to the propeller swirl that modifies the local wing angle of attack in the propeller region of influence is evident. The reference line representing the clean aircraft case (no propeller installed) allows to distinguish the effects of the nacelle and of the propellers. Small differences are also visible in the loads of the inboard wing, up to around mid-span, for the same propeller rotation in the case of co-rotating and counter-rotating layouts. This suggests that for accurate load predictions both propellers must be considered and studying an isolated wing with propeller may not be enough. Overall, the total average lift of the three configurations is quite similar: the counter-rotating top-in option gives 1.16% less than the co-rotating option, while the counter-rotating top-out option 1.19% more. As a

measure of the aerodynamic efficiency of the various installation layouts, Table 5 presents the lift over drag ratio for each case. In line with previous studies[5], the counter-rotating top-out configuration appears to be the best design choice from the aerodynamic point of view. This is mainly due to the reduction of the drag pressure component (-0.81% with respect to the co-rotating layout), in conjunction with the above mentioned lift increase.

	CO	**CNTI**	**CNTO**
Lift/Drag	20.324	20.171	20.644

Table 5: Aerodynamic efficiency for the different installation layouts.

Propeller Loads Analysis. The presence of the nacelle and the wing also affects the propeller, yielding a periodic blade load variation during a propeller revolution. To visualize the effects of the installation, Figure 7 shows the propeller loads as function of the blade azimuthal position ψ for the co-rotating layout. Thrust and torque coefficients display the largest deviations from isolated axial flight values as the blade passes in front of the wing. Any deviation from symmetry observed between the up- and down-stroking blades is due both to the asymmetric wing profile, and to the lack of axial propeller inflow. In particular, because of the negative incidence of the propeller rotational axis (see Table 3), the up-stroking blade experiences a higher local angle of attack, thus resulting in higher loads. It is therefore expected that the inboard-up propeller installation option generates louder loading noise. This choice also shows a slightly higher propeller efficiency, although propeller operating conditions do not vary significantly in the cases of inboard-up or inboard-down rotation. Overall, the propeller installed at the tested fixed-pitch cruise conditions gives about $2.7\% - 2.8\%$ more thrust than the propeller in isolation at axial flight conditions, with a penalty in the efficiency of about $0.6\% - 0.7\%$ due to an increase in torque of about 3.4%.

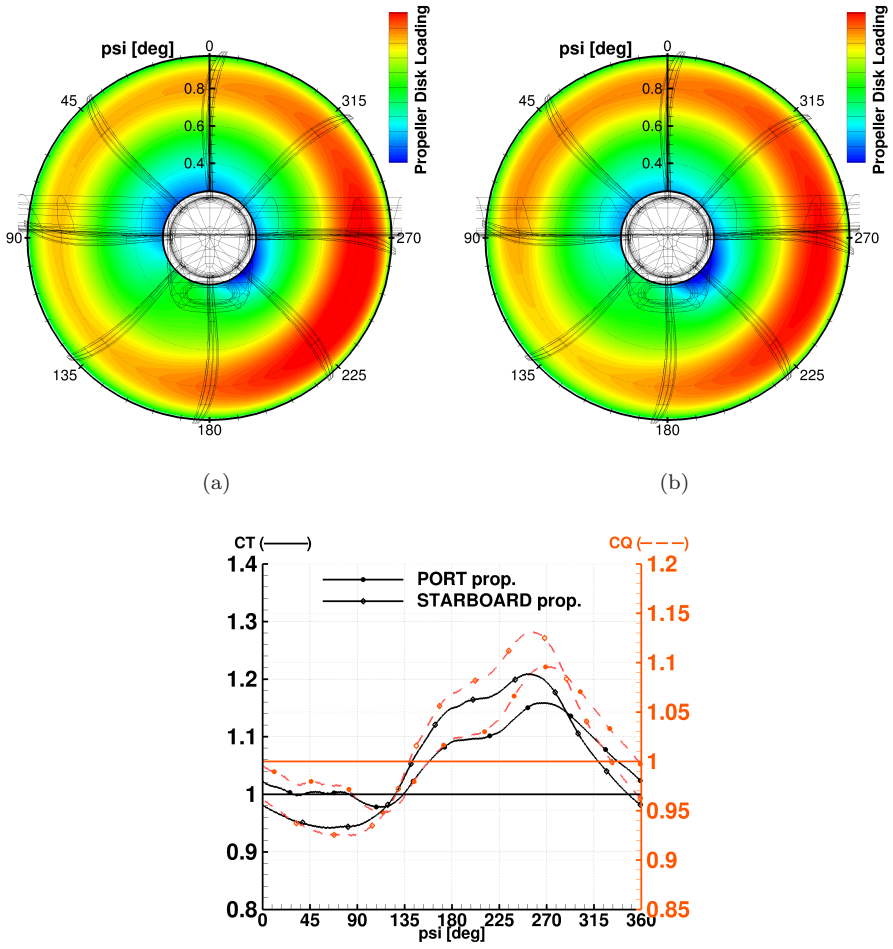

(a) (b)

(c)

Figure 7: Installation effects on the propeller loads - **CO**. (a) Disc thrust loading for the starboard propeller, i.e. inboard-up rotating propeller (frontal view). (b) Disc thrust loading for the port propeller, i.e. inboard-down rotating propeller (frontal view). (c) Thrust and torque coefficients progress during a full propeller revolution for one blade. Results are scaled with respect to the corresponding values for the isolated propeller in axial flight.

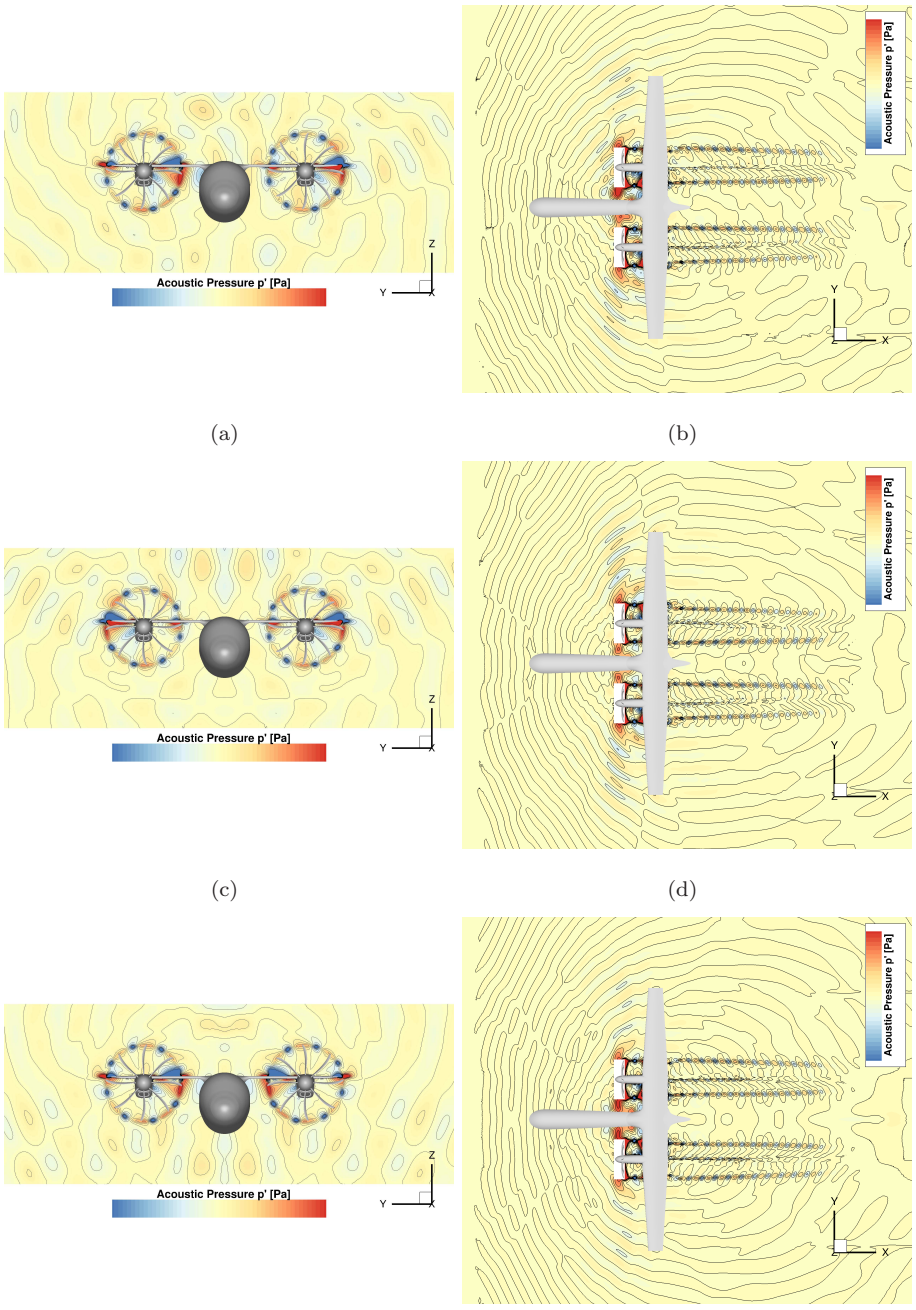

Figure 8: Instantaneous unsteady pressure field visualization: comparison between the different installation configuration, $\psi_b = 90$ deg. Transversal plane at $\sim 1R$ behind the propeller plane on the left, longitudinal plane at propeller spinner height on the right. (a),(b) **CO**. (c),(d) **CNTI**. (e),(f) **CNTO**.

4.1.2. Acoustic Analysis

Aircraft External Sound Field. Figure 8 shows the instantaneous unsteady pressure field for different layouts on transversal and longitudinal planes. The adopted mesh resolution captures the pressure perturbations generated by the propeller blade tips and the propagation of the associated acoustic waves further down-stream, up until the rear end of the fuselage.The interaction of the sound waves with the wings is visible and noise travelling in the up-stream direction, as well as emitted from the back of the nacelles, can be also noticed. As for the aerodynamics, the acoustic field for the counter-rotating layouts is symmetric, while differences between aircraft port and starboard sides are evident in the case of co-rotating propellers. The pressure perturbations generated by the interaction of the blade tip vortices with the wing leading-edge appear significantly larger on the up-stroking blade side, because of the higher loads of both blade and wing. Moreover, from time visualizations of the unsteady pressure, the sound waves emitted here are seen to be reflected by the nacelle and to interfere constructively with the direct sound field generated by the propeller rotation. The result is perturbations of larger amplitude in the wing-fuselage junction area for inboard-up propeller rotation. In the case of co-rotating propellers, the wave front propagating up-stream after the reflection on the fuselage starboard wall is also seen considerably stronger, whereas for counter-rotating top-out propellers some favorable (destructive) acoustic interferences yield smaller amplitudes. Therefore, louder noise is expected in the aircraft cabin when the propeller rotates inboard-up, especially in the case of co-rotating propellers layout.

The unsteady pressure distribution on the aircraft for a fixed instant, and the resulting overall sound pressure levels, are shown in Figures 9 and 10, respectively. Pressure perturbations due to the impact of the propeller wake on the wing leading edge are visible. Differences between the wing side in the propeller up-wash and that in the propeller down-wash are evident. The first shows fluctuations of larger amplitude, as expected from the acoustic field analysis,

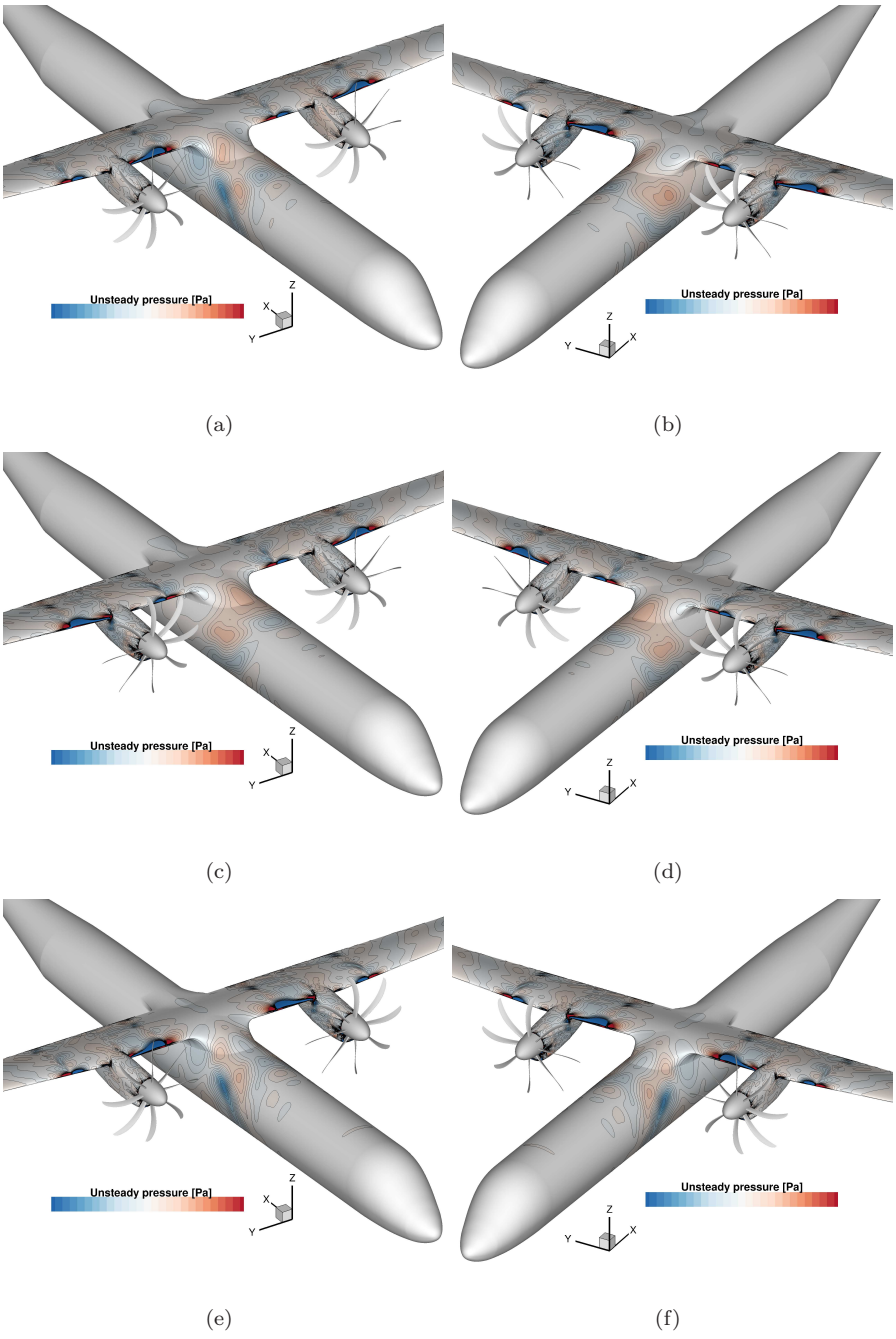

Figure 9: Unsteady pressure field on the aircraft, instantaneous visualization ($\psi_b = 90$ deg) for the different layouts. View of the starboard side on the left and of the port side on the right. (a),(b) **CO**. (c),(d) **CNTI**. (e),(f) **CNTO**.

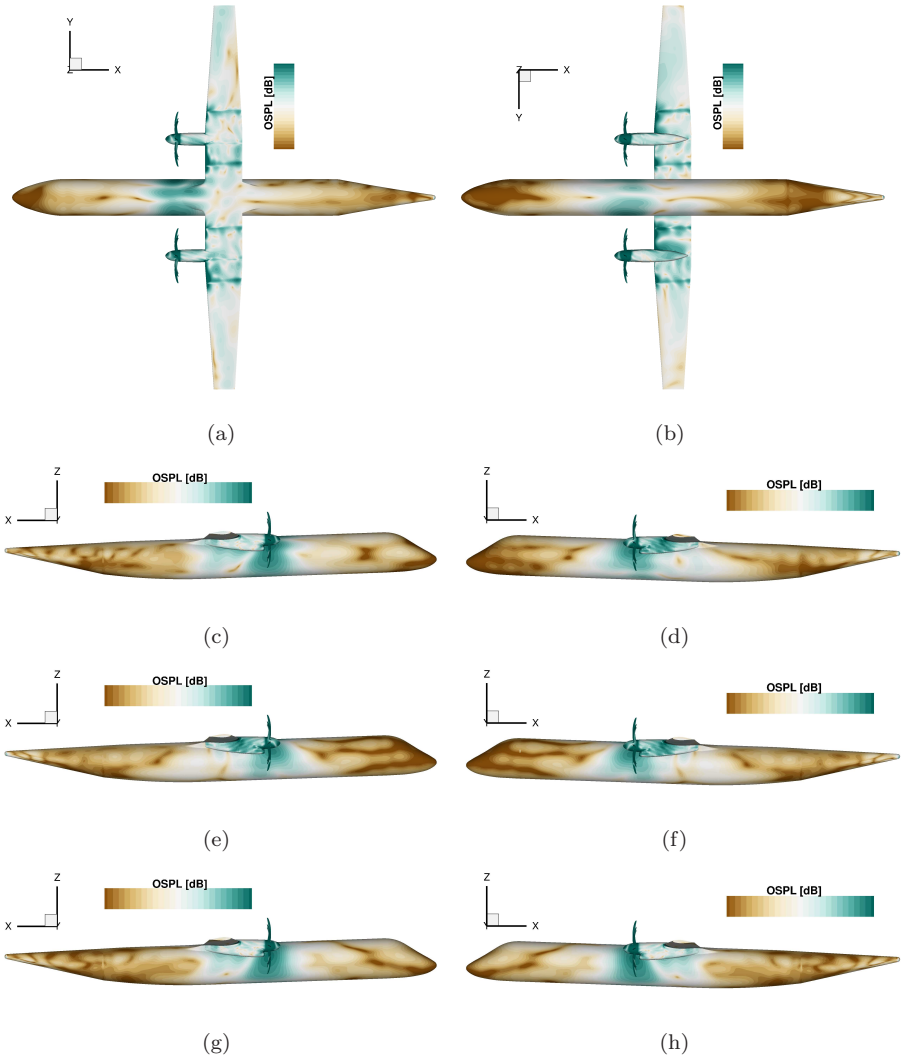

Figure 10: OSPL on the aircraft external surface for the different layouts (noise estimate from URANS results over a quarter of propeller revolution). Color scale range equal to 45 dB. (a) **CO**: top view. (b) **CO**: bottom view. (c) **CO**: starboard side. (d) **CO**: port side. (e) **CNTI**: starboard side. (f) **CNTI**: port side. (g) **CNTO**: starboard side. (h) **CNTO**: port side.

and produces, in the case of inboard-up propeller rotation, a large area of high noise on the wing's lower surface near the nacelle attachment. Footprints of the tip blade vortices can also be noted on the wing, on both the upper and the lower wing surfaces, at the boundary of the propeller slipstream. Pressure fluctuations associated with the blade root vortices are also solved by the simulation and noticeable on the front part of the nacelles. On the aircraft fuselage, significant pressure perturbations, and thus the highest sound levels, are observed in proximity to the propeller plane, from about one propeller radius upstream up to the wing trailing edge station. The aircraft port and starboard sides display, as expected, a symmetric noise field for the counter-rotating propellers layouts, while differ for the co-rotating configuration. Differences in the OSPL distribution between the cases of inboard-up and inboard-down rotating propeller are evident, with the second option appearing beneficial. Differences can also be seen in unsteady pressure and OSPL on the fuselage for the same propeller rotation but different installation option (i.e. on the port side between co-rotating and counter-rotating top-in layouts, Figs 10(d) and 10(f), and on the starboard side between co-rotating and counter-rotating top-out layouts, Figs 10(c) and 10(g)). This proves that the interaction of the acoustic fields of the two propellers is important and that the CFD method is able to resolve it. Data acquired by numerical probes are used to make a more effective quantitative comparison between the different turboprop configurations. Figure 11 shows the OSPL distribution as a function of the fuselage azimuth at the propeller plane, reporting, as a reference, the results for the isolated propeller in axial flight. The differences between isolated and installed propeller cases are substantial. The first one shows a regular distribution on the fuselage, whereas in the installed cases the interaction of the sound fields of the two propellers and the presence of the aircraft lead to an irregular noise pattern and higher noise. Results of the isolated propeller significantly underestimate the installed OSPL (up to 9 dB for positions at the passengers head height), without showing a constant shift in the predictions. Therefore, the computationally cheap simulation of a steady single blade in axial flight is not suitable for evaluating

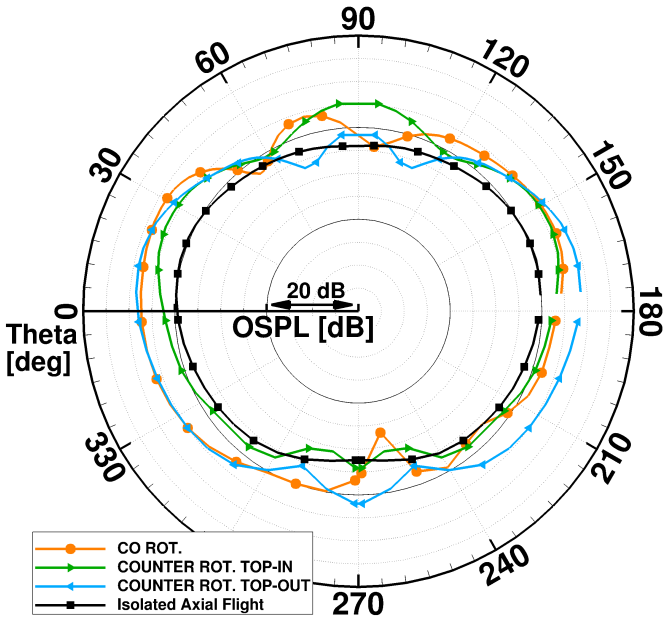

Figure 11: OSPL distribution as function of the fuselage azimuth θ at the propeller plane: comparison between the different propeller installation layouts and the isolated propeller in axial flight. Noise estimate from numerical probe data over one full propeller revolution. Refer to Figure 1(d) for the azimuthal coordinate definition.

the actual sound levels on a flying aircraft. The installed propeller cases show a local OSPL reduction around $\theta \sim$ 55-70 deg and $\theta \sim$ 95-120 deg, with the location of the minimum depending on the installation layout adopted. The resulting lobe at the top of the fuselage is centered in the cases of counter-rotating propellers, i.e. the maximum is at $\theta = 90$ deg, and moved towards the side of the inboard-up rotating propeller in the case of a co-rotating configuration. Some irregularities in the OSPL trend in the installed cases are also observed in the lower part of the fuselage (240 deg $\leq \theta \leq$ 300 deg). In the central part of the fuselage, where the aircraft masks the sound field of the second propeller, the noise distribution appears quite smooth. A noise maximum is seen around the location of minimum distance between propeller and aircraft, whose position depends on the propellers configuration, followed by a

smooth reduction going towards the bottom of the fuselage. Remarkable differences between the various installation layouts are noted and can reach up to 5 or 6 dB at certain azimuthal locations. As anticipated from the acoustic field analysis, the inboard-up propeller direction yields higher sound levels than the inboard-down. The co-rotating configuration exhibits a OSPL distribution very similar to that of counter-rotating top-out propellers on the starboard side for $\theta \leq 25$ deg and to that of counter-rotating top-in propellers on the port side for $\theta \geq 145$ deg because of the fuselage masking effect. Large differences are instead noted in the top area of the fuselage, where the sound waves from the two propellers interfere, creating a different acoustic field depending on the installation option. To investigate more in depth the differences in the OSPL between the various layouts, Figure 12 shows some of the unsteady pressure waveforms recorded by the numerical probes on the aircraft fuselage over one propeller revolution at certain angular positions at the propeller plane. A predominant eight-period oscillation related to the blade passing frequency is visible in all pressure time signals as expected. Also from the numerical probes the symmetry of the acoustic field for the counter-rotating layouts can be observed. Looking at the pressure time histories at the location near the starboard OSPL minimum for co-rotating propellers (Figure 12(a)), a smaller fluctuation amplitude for this layout can actually be seen, as well as the presence of the second harmonic frequency. This indicates that the sound waves propagating from the propeller to the fuselage wall undergo some favorable interactions with other sound waves, probably waves emitted by the airframe since the sound travelling time from the wing leading edge to the fuselage is close to the blade passing time. At the same azimuthal location, on the port side (Figure 12(b)), the scenario for the co-rotating configuration is different: the pressure history displays a smooth sinusoidal trend with an amplitude that is larger than the other installation layouts, and thus the loudest noise. Counter-rotating top-in and top-out propellers do not show significant differences at these two locations, and their signals, with respect to the co-rotating one, slightly lead on the starboard side while slightly lag on the port side.

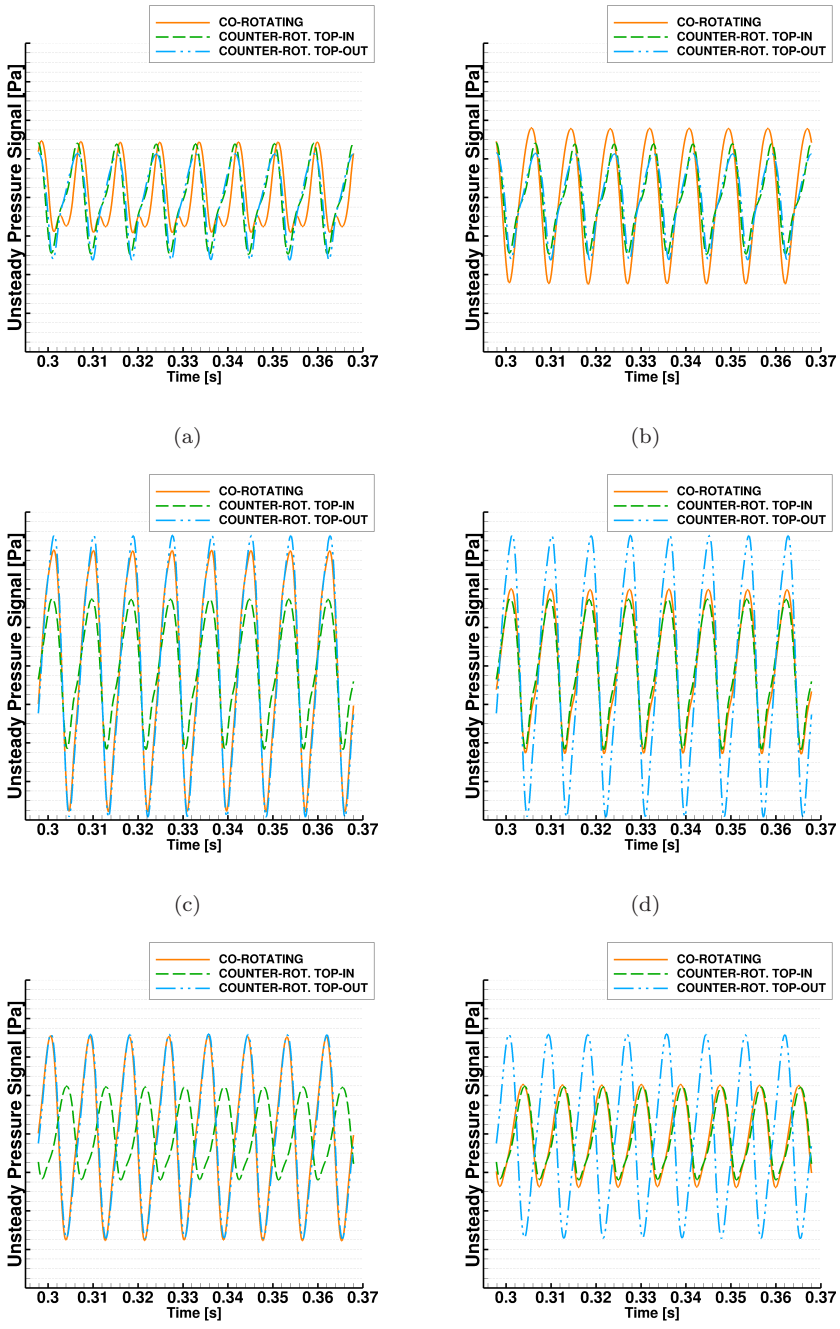

Figure 12: Unsteady pressure waveforms, for one propeller revolution, on the aircraft fuselage at the propeller plane, for some angular positions: comparison between the different propeller installation layouts. Data from numerical probes for the last full propeller revolution run. See Figure 1(d) for the azimuthal coordinate definition. (a) $\theta = 57$ deg. (b) $\theta = 123$ deg. (c) $\theta = 358$ deg. (d) $\theta = 178$ deg. (e) $\theta = 325$ deg. (f) $\theta = 205$ deg.

It is also interesting to note the flattening of the sinusoidal signal after the low-picks for about half of the oscillation amplitude for both counter-rotating propeller cases, suggesting the existence of acoustic interferences between various sound sources. Near the fuselage centerline (Figures 12(c) and 12(d)) the main difference between the three installation options is the magnitude of the pressure fluctuations, significantly larger in the case of inboard-up propeller rotation. No difference in phase is detectable between the three pressure histories. The signal flattening after the low-picks appears at this azimuthal position only in the case of inboard-down propeller rotation, i.e. for the counter-rotating top-in layout on both fuselage sides and for the co-rotating layout on the starboard side, but covering a smaller part of the signal. At lower fuselage positions (Figures 12(e) and 12(f)), differences both in amplitude and phase between inboard-up and inboard-down rotating propeller cases are significant. The flattening of the signal progressively reduces moving towards the bottom of the fuselage, disappearing faster in the co-rotating propeller case.

As shown in Figure 11, at the propeller rotational plane, apart from the upper part of the fuselage, the counter-rotating top-out layout appears the loudest option, while the counter-rotating top-in layout appears the quietest. To evaluate overall the acoustics of the various configurations, in Figure 13, the sound levels on the aircraft fuselage are compared at different stations in the area where the higher OSPL is observed. Going up-stream of the propeller's rotational plane (Figures 13(a),13(c) and 13(e)), the OSPL distribution on the fuselage shows the same trend, with a maximum around the points closer to the propellers, two local minima at about $\theta \sim 60$ and 120 deg for counter-rotating propellers and at $\theta \sim 60$ and 100 deg for co-rotating propellers, a lobe at the top of the fuselage and a noise reduction at the bottom. The larger the distance from the propeller rotational plane, the lower the noise, as could be expected. The noise reduction at the local minima at $\theta \sim 60$ and 100-120 deg increased as well. The differences between the different layouts in the OSPL trend in the upper fuselage area become more significant, the counter-rotating top-in configuration showing the quietest noise.

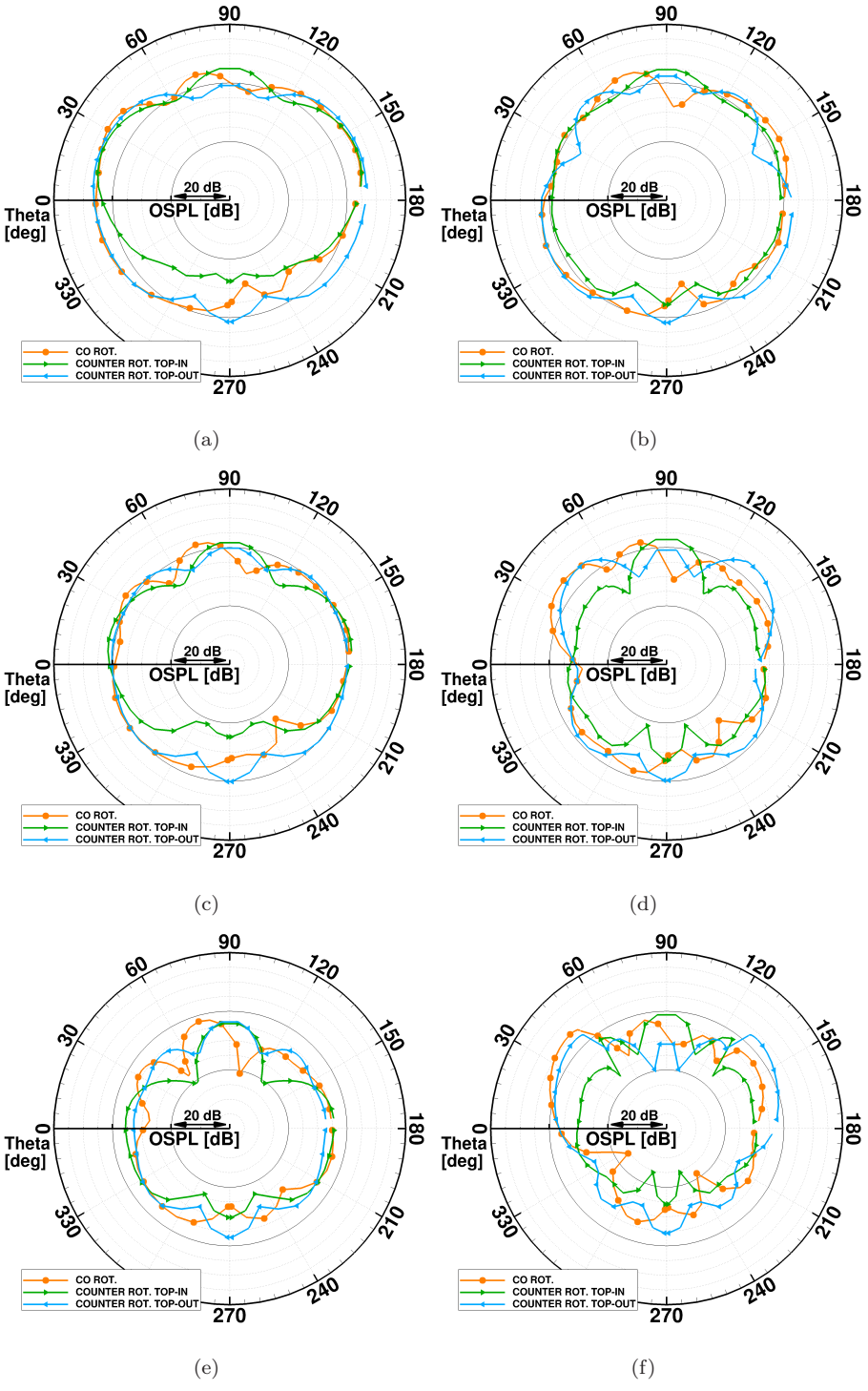

Figure 13: OSPL on the fuselage as a function of the angular position at various fuselage stations: comparison between the different propeller installation layouts. Noise estimate from numerical probe data over one full propeller revolution. Refer to Figure 1(d) for the azimuthal coordinate definition. (a) $X \sim -0.8$ m. (b) $X \sim +0.8$ m. (c) $X \sim -1.5$ m. (d) $X \sim +1.5$ m. (e) $X \sim -2.2$ m. (f) $X \sim +2.2$ m.

The differences amongst the various configurations in the lower area of the fuselage, instead, decrease when going away from the propeller rotational plane. For up-stream distances greater than R/2 (Figures 13(c) and 13(e)) the pick of the upper lobe tends to the same sound level in the cases of counter-rotating layouts, while near the propeller rotational plane a difference up to 5 dB is predicted, in favor of the counter-rotating top-out option. Moreover, at these distances, the co-rotating propeller configuration shows a second local minimum of the OSPL on the starboard side around $\theta \sim 5$ deg which is not present in the other two installation options and makes this layout the quietest at this specific location. Moving down-stream from the propeller rotational plane (Figures 13(b),13(d) and 13(f)), due to the airframe sound waves reflections and connected interactions with the incoming acoustic waves, the OSPL distribution on the fuselage is different than ahead of the propeller plane, and its azimuthal trend becomes more irregular. Besides the points of local minimum defining the lobe at the top of the fuselage, other OSPL valleys can be seen on the upper-half of the fuselage creating one couple of additional lateral lobes, or two in proximity of the wing junction. The magnitude and the azimuthal positions of the main lateral lobes peak, as well as their extension, are shown to vary with the fuselage station. Increasing the distance from the propeller rotational plane, the differences in the OSPL predicted for the various layouts become larger and substantial: up to 10 dB of difference are observable for some azimuthal locations around $R/2$ away from the propeller plane (see Figure 13(d)) and up to 15 dB about one radius away (see Figure 13(f)). The counter-rotating top-in option appears overall the quietest, even though the counter-rotating top-out configuration shows significantly lower noise for the top lobe. Inboard-up rotating propellers yield to lateral lobes considerably louder and covering a larger fuselage surface than inboard-down rotating propellers. Moreover, when the co-rotating layout is adopted, the lateral lobe on the side of the inboard-up rotating propeller is observed to give highest OSPL than when counter-rotating top-out propellers are employed, suggesting a detrimental acoustic interaction in the first case. The noise attenuation moving away from the propeller rotational

plane is less than the one observed going up-stream because of the airframe reflections, except for the counter-rotating top-in layout that exhibits, at equal distances from the propeller plane, lower OSPL down-stream than up-stream. As for fuselage stations ahead of the propeller plane, the local point of OSPL reduction in the half-lower part of the starboard side is more pronounced for the co-rotating propeller configuration. Finally, it is pointed out that, for all fuselage stations, at the locations of the OSPL local minimum, the frequency of the second tone is also observable in the pressure signal, indicating that important noise cancellations are generated by the interactions of propeller and airframe sound waves.

Cabin Internal Noise. As an example of the transfer function application, the unsteady pressure amplitude maps in the frequency domain, outside and inside the fuselage shell, are presented in Figure 14 for the fundamental harmonic. The modifications of the pressure field going through the fuselage shell, and the non-uniformity of the transmission losses of the aircraft structure, are noticeable. Whereas the exterior unsteady pressure distribution shows marked differences depending on the propeller rotation, with the inboard-up case yielding fluctuations of higher amplitude and over a larger area of the fuselage surface, on the inside the unsteady pressure field presents more similar characteristics for all propeller installation layouts. In the cabin interior, because of the filtering properties of the aircraft shell, differences of the various configurations concern mainly the pressure oscillations magnitude.

The resulting pressure history for the test passenger is shown in Figure 15(a), together with the pressure signals at the same fuselage station and the same height on the external fuselage surface. The amplitude of the pressure fluctuations decreases considerably between outside and inside the aircraft cabin. In the transmission across the fuselage shell the acoustic perturbations are reduced by around $17-20$ times. Differences in the pressure oscillations among the various installation layouts are maintained and are of the same order as those outside. The counter-rotating top-in configuration shows the smaller pressure

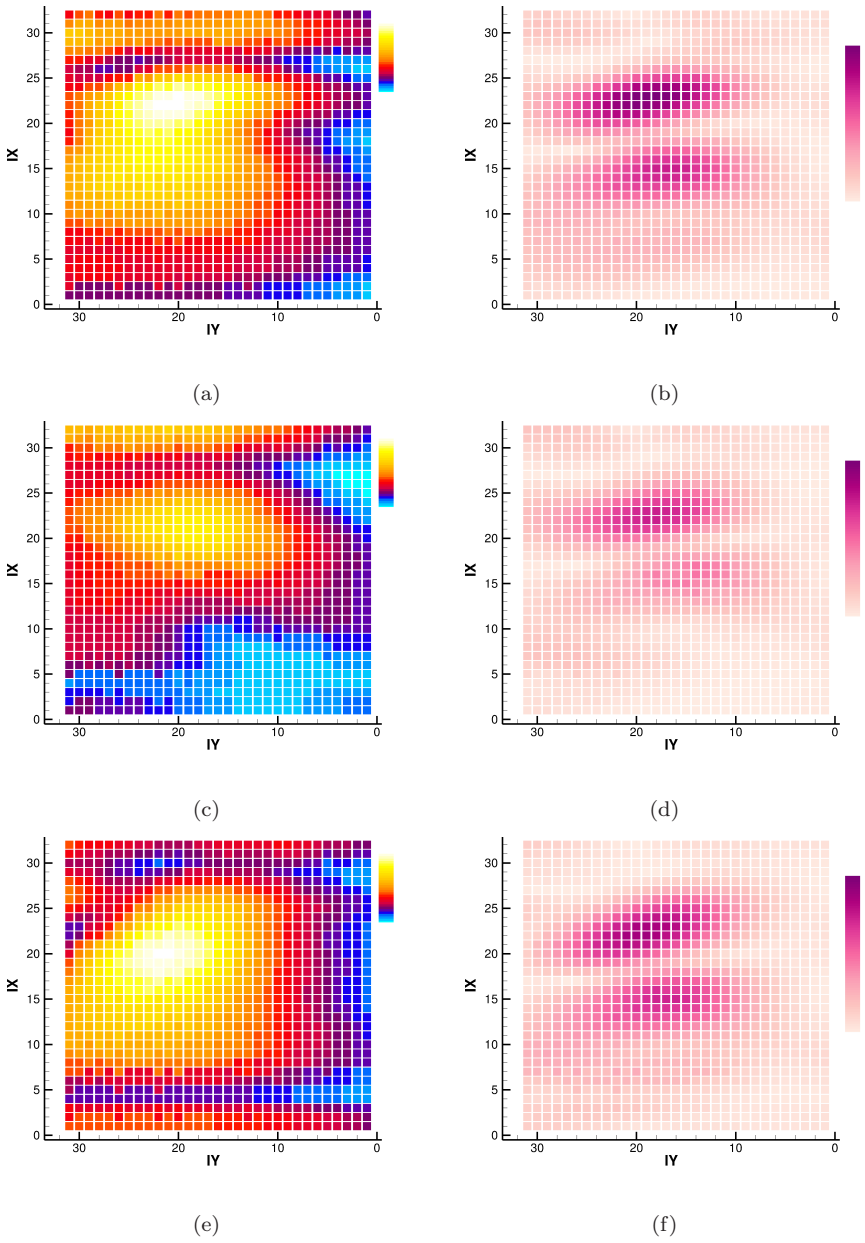

Figure 14: Transfer functions application for the different installation layouts: unsteady pressure amplitude maps at f = BPF on the fuselage exterior surface (on the left) and the corresponding internal one (on the right). Please refer to Figure 2(c) for the definition of the coordinate IX and IY used for the plots and the TF area location. (a),(b) **CO**. (c),(d) **CNTI**. (e),(f) **CNTO**.

fluctuations magnitude, indication of quieter sound levels. The cases of counter-rotating top-out and co-rotating propellers have very similar pressure signals, the clear differences in the exterior acoustic field are probably attenuated in the transmission through the fuselage.

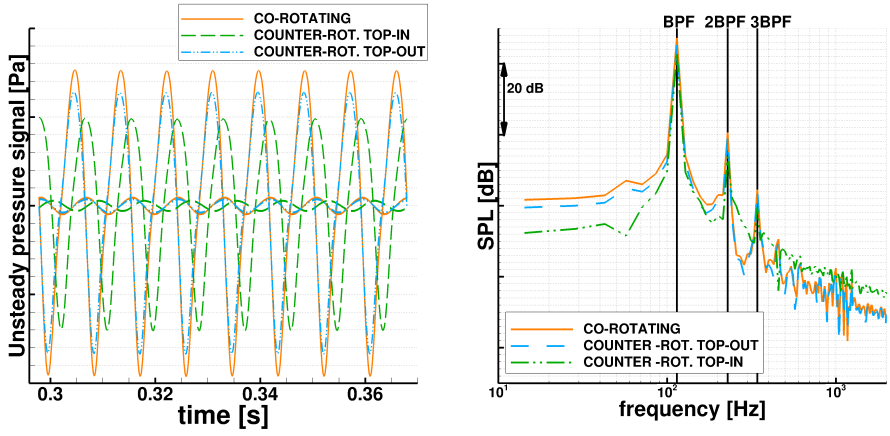

(a) (b)

Figure 15: Cabin interior sound evaluation using experimental TF: comparison between the different propeller installation options. Data refer to a passenger located on the starboard side of the airplane, slightly ahead of the propeller rotational plane. (a) Unsteady pressure signal (thick lines) compared with the one at the same height on the external fuselage surface (thin lines). (b) Sound Pressure Level spectra in the frequency domain.

The sound spectra in the frequency domain for the test passenger are reported in Figure 15(b). The tone at the blade passing frequency dominates the noise content. Components at the second and third propeller harmonics are also visible in the spectra. The counter-rotating top-in configuration appears to be the quietest, while the co-rotating the loudest. At the fundamental frequency, the predicted SPL for the co-rotating layout is around 2 and 4 dB higher than the counter-rotating top-out and top-in options, respectively. At 2 BPF, differences between co-rotating and counter-rotating top-out configurations become smaller, whereas the counter-rotating top-in option shows a benefit of more than 6 dB.

In conclusion, from the acoustic analysis carried out, the counter-rotating top-in configuration appears the best design choice from the acoustic point of view, if the two propellers do not have any shift in phase.

4.2. Assessing of Synchrophasing

4.2.1. Aerodynamic Analysis

For brevity, aerodynamic considerations are here omitted, since these are discussed for the different installation layouts above. It is only noted that: *(i)* all synchrophased configurations provide a total thrust and a total lift that differ by less than 0.1% with respect to the case of propellers in phase; *(ii)* interestingly, for some synchrophase angles, the loads fluctuations on the starboard wing show not only a phase shift but also a different magnitude.

4.2.2. Acoustic Analysis

Aircraft External Sound Field. The OSPL distribution on the aircraft fuselage is shown in Figure 16 for the synchrophase angles considered. Although the general trend of the noise field remains substantially the same, some differences can be observed. On the starboard side, there is a slight change in the azimuthal position and extent of the longitudinal noise lobe (A); the main noise lobe (B) is also seen to vary its size and the azimuthal location of its peak. Looking further aft, no significant differences are noted in the fuselage region below the wing (C), while sound levels and the position of the noise minimum behind the wing (D) are altered depending on the synchrophase angle. Regarding the fuselage frontal area (E), a similar noise pattern is observed in all cases, with small variations in sound levels, except for the configuration with $\psi_s = 30$ deg that shows an OSPL distribution considerably different. Smaller differences are registered on the port side among the cases of $\psi_s = 5$, $\psi_s = 10$ and $\psi_s = 15$ deg, whereas the choice of $\psi_s = 30$ deg results in a more extended area of high noise in the vicinity of the propeller plane (A) and a different OSPL pattern at the back (C) and front (D) of the fuselage. Finally, since the OSPLs of $\psi_s = 15$ deg and $\psi_s = 30$ deg (or $\psi_s = -15$ deg equivalently) are dissimilar, the developed

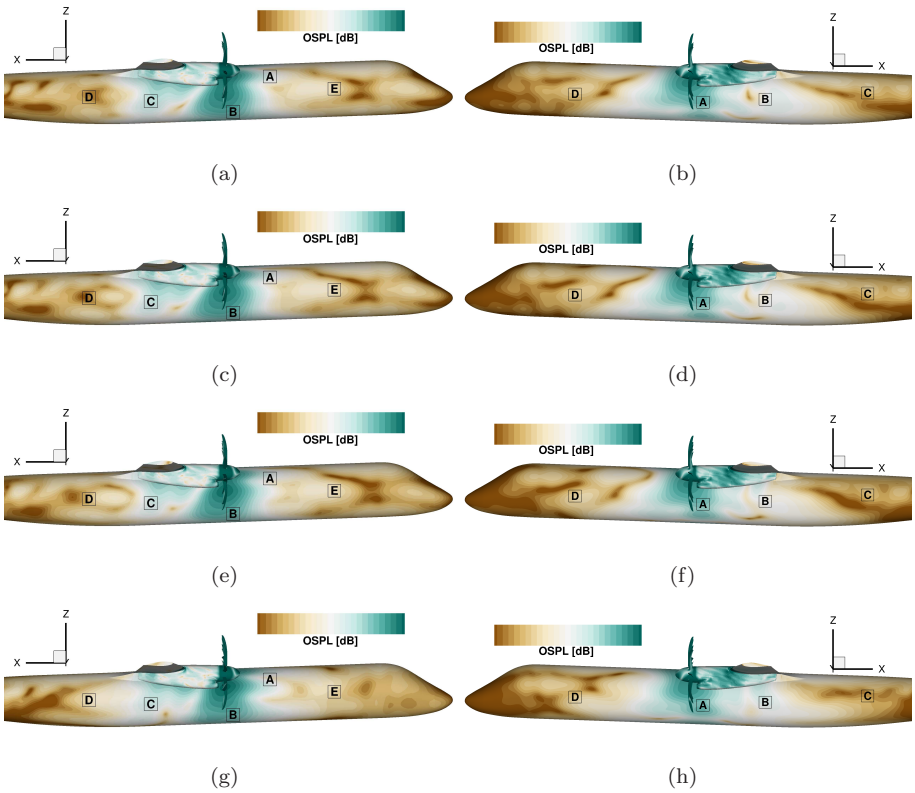

Figure 16: OSPL on the aircraft external surface for the different cases (noise estimate from URANS results over a quarter of propeller revolution). Color scale range equal to 45 dB. Aircraft starboard side on the left and port side on the right. Refer to Figure 10 for the case of propellers in phase. (a),(b) $\psi_s = 5$ deg. (c),(d) $\psi_s = 10$ deg. (e),(f) $\psi_s = 15$ deg. (g),(h) $\psi_s = 30$ deg.

acoustic field depends not only on the magnitude of the blade shift but also from the leading or the lagging of the starboard propeller.

Data from the numerical probes on the fuselage are used to have a better quantitative assessment of the several shift angle choices. Figure 17 presents the OSPL as a function of the fuselage azimuthal position, at different longitudinal stations. The corresponding data for the case of propellers in phase are included for comparison. In general, the main effect of the positive synchrophase angle appears to be a shift of the noise pattern towards slightly larger fuselage az-

imuthal angles, as can be seen looking at the position of the noise lobe on the upper part of the fuselage.

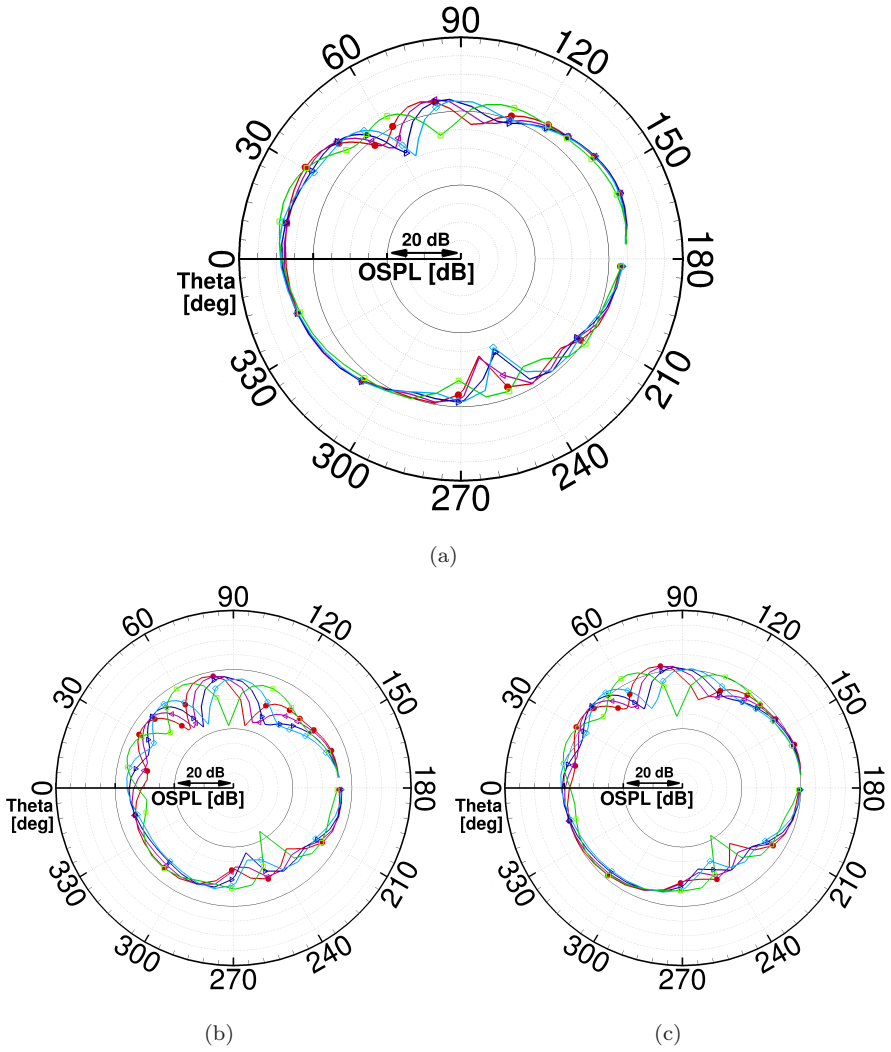

(a)

(b) (c)

Figure 17: OSPL around the fuselage at various streamwise stations: comparison between the different test cases. Noise estimate from numerical probe data over one full propeller revolution. Refer to Figure 1(d) for the azimuthal coordinate definition. Red plain circles - $\psi_s = 0$ deg; purple left triangles - $\psi_s = 5$ deg; blue right triangles - $\psi_s = 10$ deg; cyan diamonds - $\psi_s = 15$ deg; light green squares - $\psi_s = 30$ deg. (a) $X \sim 0.0$ m. (b) $X \sim -2.0$ m. (c) $X \sim -1.5$ m. *Continued in the next page*

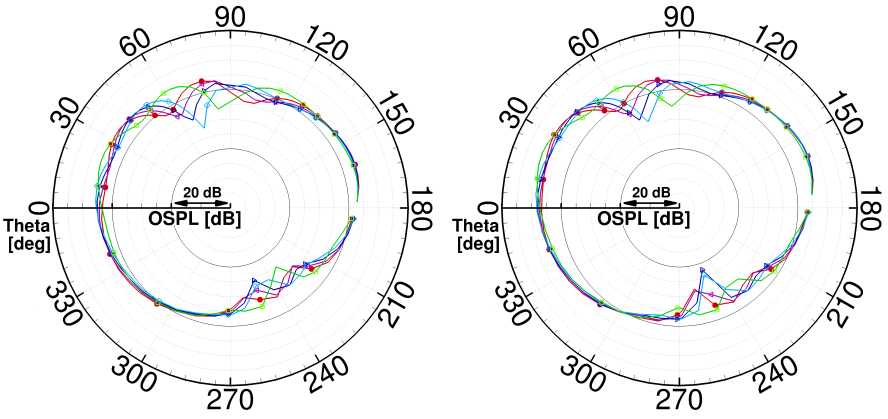

(d) (e)

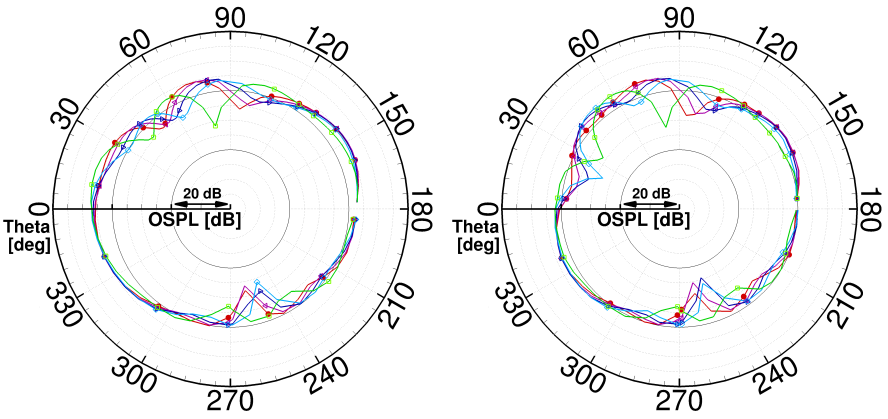

(f) (g)

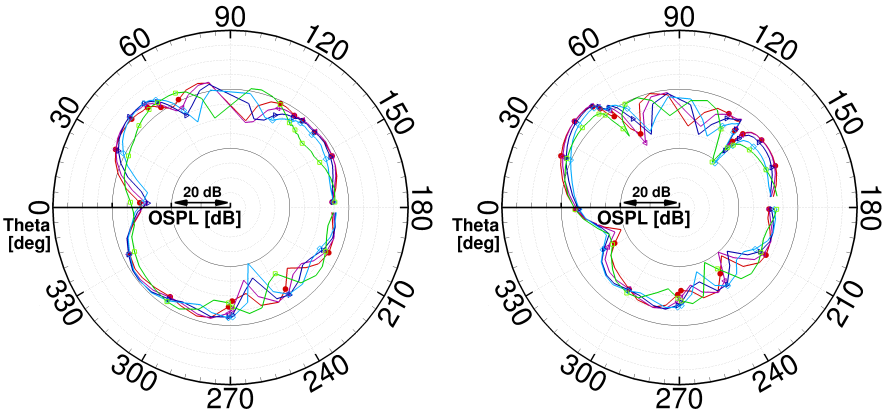

(h) (i)

Figure 17: (d) $X \sim -1.0$ m. (e) $X \sim -0.5$ m. (f) $X \sim +0.5$ m. (g) $X \sim +1.0$ m. (h) $X \sim +1.5$ m. (i) $X \sim +2.0$ m.

For fuselage stations ahead of the propeller and up to around one propeller radius behind it, the differences in the sound levels of the noise maximum are at most of 2 dB. Bigger differences are instead observed regarding the points of minimum noise, where the configurations with synchrophasing show reductions of up to 5 dB more than the case of propellers in phase, indicating a stronger noise destructive interference. Further back, where the noise on the fuselage is also affected by the acoustic waves generated by the interactions with the airframe, the noise distribution is seen to vary more considerably between the various test cases. The maximum sound levels of the upper-lateral lobes, both on the starboard and the port side, are observed to decrease with a positive increase of the synchrophase angle.

To assess overall the acoustics of the various options, Figure 18 shows the trend of the OSPL averaged over the azimuth, along the fuselage longitudinal axis. The average value for the OSPL, at each fuselage station, was computed taking into account only the upper part of the fuselage and excluding the data relative to the area below the cabin floor. Thus, the variations in the OSPL between $\theta \sim 240$ and $\theta \sim 270$ deg are not included. As can be noted, ahead of the propeller tip plane, all cases present very similar noise values, with some differences only for distances larger than one propeller diameter. The case of $\psi_s = 30$ deg is, however, an exception. This synchrophase angle, which is larger than the maximum possible blade shift, yields slightly higher OSPL for the whole front part of the aircraft fuselage. Behind the propeller plane, the effect of the blade shift is more considerable, and differences between the various configurations increase the closer we are to the wing-fuselage junction. This indicates that propellers synchrophasing modifies not only the acoustic interference that develops between the sound fields of the two propellers, but also, and in greater ways, the interference of the propellers direct sound fields with the one produced from the interactions with the airframe. It appears therefore crucial, when studying the optimum synchrophase angle numerically, to include the airframe in the simulations. Any tested synchrophase angle shows a beneficial effect in this area of the fuselage, with noise reductions of up to 1 dB about

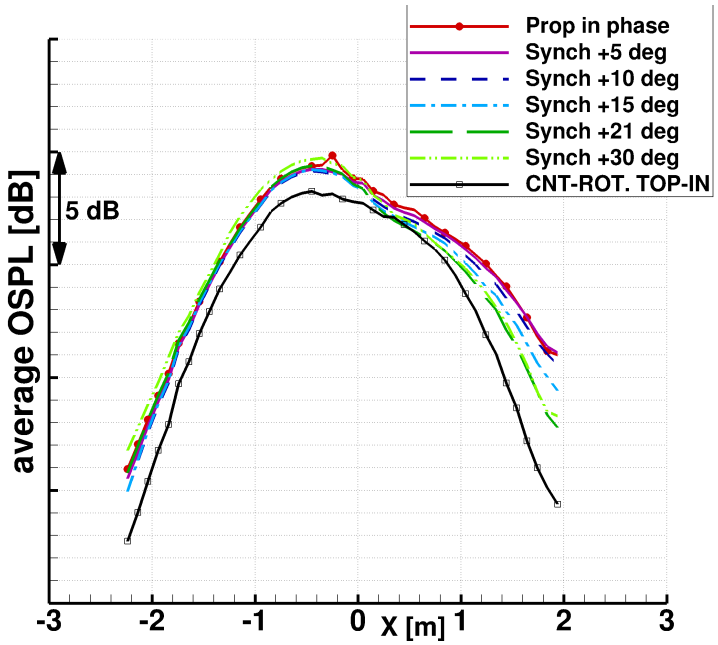

Figure 18: OSPL averaged over the fuselage azimuth θ, in the passengers area, as a function of the fuselage longitudinal position: comparison between the different test cases and counter-rotating top-in scenario as a reference. Noise estimate from numerical probe data over one full propeller revolution.

half radius away from the propeller plane and up to about 2 dB one radius away. Larger synchrophase angles provide larger noise reductions. The OSPL decrease is seen to be non-linear with respect to the synchrophase angle. The choice of $\psi_s = 15$ deg appears overall the quietest amongst the synchrophase angles considered. Finally, in the same graph is reported, as reference, the OSPL trend for the counter-rotating top-in propeller installation layout, which was proven the quietest option in the first part of this study. At all fuselage stations, no synchrophase angle is able to achieve a noise reduction equal to that obtained by the top-in propellers rotation. Table 6 reports the overall (i.e. for the fuselage region from 1 radius ahead the propeller tip plane to the wing-fuselage junction) noise gains that are attained with synchrophasing compared to in-phase propellers. The value for the counter-rotating top-in propellers layout is re-

$\psi_s = 5$ deg	$\psi_s = 10$ deg	$\psi_s = 15$ deg	$\psi_s = 30$ deg	CNTI Layout
- 0.16 dB	-0.365 dB	-0.55 dB	-0.36 dB	-2.17 dB

Table 6: OSPL average value for the fuselage region from 1 radius ahead the propeller tip plane to the wing-fuselage junction: relative value with respect to the case with propellers in phase ($\psi_s = 0$ deg). Value of the counter-rotating top-in (CNTI) layout reported as reference. Data from numerical probes over the last full propeller revolution. The lower part of the fuselage (below the cabin floor) was not considered.

ported as a target. All synchrophase angles analyzed lead to a reduction in the OSPL. If the gain obtained by a choice of $\psi_s = 5$ deg appears quite negligible, with $\psi_s = 15$ deg it is possible to achieve a noise reduction of more than 0.5 dB with respect to in-phase propellers. The option of $\psi_s = 30$ deg seem to not be optimal because the considerably larger gain provided in the area between the propeller plane and the wing-fuselage junction comes together with an increase in the sound levels ahead the propeller plane.

Looking at the average OSPL as a function of the synchrophase angle, it can be imagined that a choice closer to the maximum possible blade shift, i.e. $\psi_s \sim 22.5$ deg, may yield larger noise reductions. For this reason an additional simulation was performed with $\psi_s = 21$ deg (considering the capability of current synchrophaser systems to maintain a shift angle within ± 1 deg, this choice was made to ensure that the starboard propeller is always leading with respect to the port one). The average OSPL along the fuselage, reported in Figure 18, displays significant benefits behind the propeller plane, showing similar sound levels to the $\psi_s = 30$ case, and a trend very close to that of propellers in phase ahead of the propeller plane. Overall, the choice of $\psi_s = 21$ deg appears the quietest co-rotating configuration, leading to a noise reduction of 0.7 dB with respect to phased propellers. However, it is noted that the acoustic gains achieved by synchrophasing are significantly lower than that obtained by the counter-rotating top-in layout.

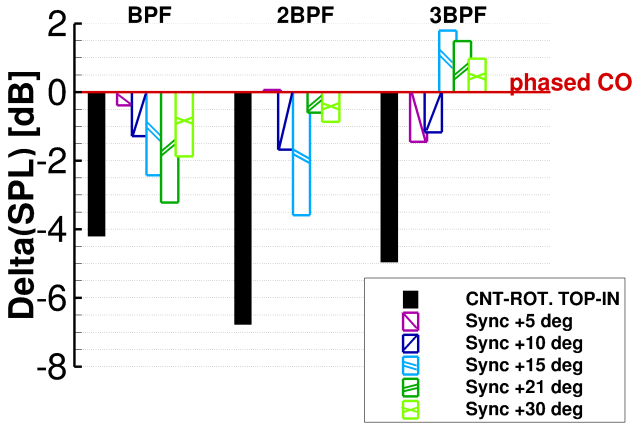

Figure 19: Cabin interior sound evaluation using experimental TF: comparison between the different cases. SPL comparison for first, second and third tone (relative data with respect to the case with propellers in phase $\psi_s = 0$ deg). Data refer to a passenger located on the starboard side of the airplane, slightly ahead of the propeller rotational plane.

Cabin Internal Noise. Figure 19 compares, for all test cases, the SPL for the first three propeller harmonics as would be heard by the example passenger. Even if the differences that appear on the external surface of the fuselage are not very strong, synchrophasing has an noticeable beneficial effect inside the cabin (apart from the case of $\psi_s = 5$ deg that appears almost not effective). The only considered shift angle that exhibits a sound levels reduction at all first three harmonics is $\psi_s = 10$ deg, but its noise gains for the first tone is significantly weaker than those achieved by $\psi_s = 15$ deg and $\psi_s = 21$ deg. The latter shows the larger reduction at the first harmonic (-3.2 dB with respect to phased propellers), while the choice of $\psi_s = 15$ is the best for the second harmonic (-3.6 dB with respect to phased propellers). Overall, the synchrophase angle equal to $\psi_s = 21$ deg gives the quietest sound levels, resulting the most favorable angle amongst those analyzed regarding both exterior and interior noise, at example passenger location. It has to be noted that the overall noise reduction provided by the counter-rotating top-in propeller layout is higher than that of the best synchrophase angle by about 1 dB.

5. Conclusions

The CFD flow solver HMB3 was successfully employed to simulate a complete twin-engined modern turboprop aircraft, aiming to numerically investigate the effects of the propeller installation options (co- vs counter-rotating propellers), and synchrophasing, on the near-field aircraft acoustics. The eight-bladed IMPACTA propeller, representative of a modern propeller design, was employed for this study and cruise conditions were considered. Noise on the exterior fuselage surface was directly evaluated from the URANS solutions, whereas experimentally-obtained transfer functions were employed to estimate the cabin noise, thus to perform an overall assessment of the acoustic field of each configuration seeking the quieter propeller installation layout. The adopted method is able to capture the aerodynamic and the acoustic features of the complex flow-field that is generated from the interactions between propellers and airframe. The interference between sound waves of the two propellers and the waves reflected from the airframe appears to play an important role in the resulting acoustic field, showing the need to simulate the whole configuration to achieve accurate actual noise estimates for an aircraft in flight.

Significant differences in the exterior acoustic field between co- and counter-rotating propellers are observed. These differences remain audible in the aircraft cabin, although significantly attenuated because of the fuselage shell filtering. Overall, if the counter-rotating top-out layout displays the best aerodynamic efficiency in line with previous studies, the counter-rotating top-in configuration is shown to be the best from the acoustic point of view at this flight condition. The propeller inboard-up rotation yields to louder noise than the inboard-down direction because of the higher blade loading on the inboard propeller side and because of constructive acoustic interferences between direct propeller sound waves and noise emitted, as well as reflected, from the interactions with the airframe.

Propeller synchrophasing was analyzed as a way to decrease the noise of a co-rotating layout being this the usually adopted for maintenance costs and

logistical reasons. In line with previous experimental and analytical studies, synchrophasing is shown to affect only slightly the exterior OSPL distribution and values, but to be effective regarding the interior cabin noise. The noise reduction appears to be mainly due to the different acoustic interferences that develop between propellers direct sound fields and the waves emanating by the airframe. The best blades shift angle amongst those considered in this study, $\psi_s = 21$ deg, yield a decrease in the OSPL of more than 3 dB at the example passenger location, compared to the case of propellers in phase. Smaller angles were proved less effective, especially in the area between the propeller plane and the fuselage-wing junction, whereas larger angles resulted louder than phased propellers ahead of the propeller plane. However, it is noted that the counter-rotating top-in layout is quieter by almost 1 dB more with respect to $\psi_s = 21$ deg, showing that the favorable effects of synchrophasing on a co-rotating configuration can be significant but do not balance the higher sound levels generated by the inboard-up rotation of one propeller.

Acknowledgment

This research was supported by Dowty Propellers[75]. Results were obtained using the EPCCs Cirrus HPC Service (https://www.epcc.ed.ac.uk/cirrus) that is acknowledged for the time allocated.

The authors would like to thank the Principal Engineer Trevor H. Wood at GE Global Research for his inputs and advice during the development of this work. NLR is also gratefully acknowledged for the use of their experimental data. The discussions on this topic with the UK VLN members were also helpful.

References

[1] P. Argüelles, M. Bischoff, P. Busquin, B. Droste, S. R. Evans, W. Kröll, J. Lagardere, A. Lina, J. Lumsden, D. Ranque, et al., European Aeronautics: a Vision for 2020 - Meeting Society's Needs and Winning Global Leadership, Tech. rep., European Commission, Directorate General for Research and Innovation -

Advisory Council for Aeronautics Research in Europe (2001).
URL http://www.acare4europe.org/sites/acare4europe.org/files/document/Vision%202020_0.pdf

[2] T. M. Darecki, C. Edelstenne, T. Enders, E. Fernandez, P. Hartman, J.-P. Herteman, M. Kerkloh, I. King, P. Ky, M. Mathieu, G. Orsi, G. Schotman, C. Smith, J.-D. Wörner, Flightpath 2050: Europes vision for aviation. report of the high level group on aviation research., Tech. rep., ACARE (Advisory Council for Aeronautics Research in Europe) - Publications Office of the European Union, Luxembourg (2011).
URL http://ec.europa.eu/transport/sites/transport/files/modes/air/doc/flightpath2050.pdf

[3] IMPACTA - IMproving the Propulsion Aerodynamics and aCoustics of Turboprop Aircraft, (Accessed 10 February 2018).
URL http://gtr.rcuk.ac.uk/project/506AE188-48A3-4C80-B96C-40E7120FFB75#

[4] N. Bown, A. Knepper, Aircraft ad Propulsion Design Requirements for the IMPACTA Project, Tech. Rep. ITS 01675, Issue 3, Dowty Propellers (GE Aviation Systems Ltd) (2013).

[5] L. Veldhuis, Review of Propeller-Wing Aerodynamic Interference, in: ICAS - 24th International Congress of the Aeronautical Sciences, Yokohama (Japan), International Council of the Aeronautical Sciences, 2004, pp. 1–21, Paper ICAS 2004-6.3.1.

[6] SKYbrary, Critical Engine, (Accessed 10 February 2018).
URL https://www.skybrary.aero/index.php/Critical_Engine

[7] H. Breitbach, D. Sachau, S. Böhme, Acoustic challenges of the a400m for active systems, in: Smart Structures and Materials 2006: Industrial and Commercial Applications of Smart Structures Technologies, Vol. 6171, International Society for Optics and Photonics, 2006, pp. 6171041–6171048. doi:10.1117/12.658435.
URL https://doi.org/10.1117/12.658435

[8] T. Kletschkowski, Adaptive Feed-Forward Control of Low Frequency Interior Noise, Springer Netherlands, Dordrecht, 2012, Ch. Active Noise Control in a Semi-closed Interior, pp. 189–235. doi:10.1007/978-94-007-2537-9_9.
URL https://doi.org/10.1007/978-94-007-2537-9_9

[9] J. Johnston, R. Donham, W. Guinn, Propeller signatures and their use, Journal of Aircraft 18 (11) (1981) 934–942. doi:http://dx.doi.org/10.2514/3.57583.

[10] B. Magliozzi, Synchrophasing for cabin noise reduction of propeller-driven airplanes, in: 8th Aeroacoustics Conference, American Institute of Aeronautics and Astronautics, 1983, pp. 1–7, Paper AIAA-83-0717. doi:10.2514/6.1983-717.
URL https://doi.org/10.2514/6.1983-717

[11] C. Fuller, Noise control characteristics of synchrophasing. I-Analytical investigation, AIAA journal 24 (7) (1986) 1063–1068. doi:10.2514/3.9392.
URL https://doi.org/10.2514/3.9392

[12] J. Jones, C. Fuller, Noise control characteristics of synchrophasing. II-Experimental investigation, AIAA journal 24 (8) (1986) 1271–1276. doi:10.2514/3.9431.
URL http://dx.doi.org/10.2514/3.9431

[13] D. Blunt, B. Rebbechi, Propeller synchrophase angle optimisation study, in: 13th AIAA/CEAS Aeroacoustics Conference (28th AIAA Aeroacoustics Conference), American Institute of Aeronautics and Astronautics, 2007, p. 3584, Paper AIAA 2007-3584. doi:10.2514/6.2007-3584.
URL https://doi.org/10.2514/6.2007-3584

[14] R. Woodward, I. Loeffler, In-flight source noise of an advanced large-scale single-rotation propeller, Journal of Aircraft 30 (6) (1993) 918–926. doi:10.2514/3.46435.
URL https://doi.org/10.2514/3.46435

[15] R. Woodward, I. Loeffler, In-flight near-and far-field acoustic data measured on the Propfan Test Assessment (PTA) testbed and with an adjacent aircraft, Tech. Rep. NASA-TM-103719, E-6402, NAS 1.15:103719, NASA Lewis Research Center; Cleveland, OH, United States (April 1993).
URL https://ntrs.nasa.gov/archive/nasa/casi.ntrs.nasa.gov/19930017869.pdf

[16] J. Dittmar, D. Stang, Cruise noise of the 2/9th scale model of the Large-scale Advanced Propfan (LAP) propeller, SR-7A, Tech. Rep. NASA-TM-100175, E-3746, NAS 1.15:100175, NASA Lewis Research Center; Cleveland, OH, United States (September 1987).
URL https://ntrs.nasa.gov/archive/nasa/casi.ntrs.nasa.gov/19870018965.pdf

[17] R. Woodward, Measured noise of a scale model high speed propeller at simulated takeoff/approach conditions, in: 25th AIAA Aerospace Sciences Meeting, American Institute of Aeronautics and Astronautics, 1987, pp. 1–27. doi:10.2514/6.1987-526.
URL https://ntrs.nasa.gov/archive/nasa/casi.ntrs.nasa.gov/19870007155.pdf

[18] M. Dunn, G. Tarkenton, Computational methods in the prediction of advanced subsonic and supersonic propeller induced noise: ASSPIN users' manual, Tech. Rep. NASA-CR-4434, NAS 1.26:4434, NASA. Langley Research Center, Washington, United States (1992).
URL https://ntrs.nasa.gov/search.jsp?R=19920012215

[19] F. Farassat, S. Padula, M. Dunn, Advanced turboprop noise prediction based on recent theoretical results, Journal of Sound and Vibration 119 (1) (1987) 53–79. doi:https://doi.org/10.1016/0022-460X(87)90189-1.
URL http://www.sciencedirect.com/science/article/pii/0022460X87901891

[20] P. Spence, Development of a boundary layer noise propagation code and its application to advanced propellers, in: 29th Aerospace Sciences Meeting, American Institute of Aeronautics and Astronautics, 1991. doi:10.2514/6.1991-593.
URL https://doi.org/10.2514/6.1991-593

[21] D. Hanson, Near-field frequency-domain theory for propeller noise, AIAA journal 23 (4) (1985) 499–504. doi:10.2514/3.8943.
URL https://doi.org/10.2514/3.8943

[22] E. Envia, Prediction of noise field of a propfan at angle of attack, Tech. Rep. NASA-CR-189047, E-6645, NAS 1.26:189047, NASA, United States (October 1991).
URL https://ntrs.nasa.gov/archive/nasa/casi.ntrs.nasa.gov/19920004541.pdf

[23] M. Nallasamy, F. Groeneweg, Unsteady euler analysis of the flowfield of a propfan at an angle of attack, Journal of Propulsion and Power 8 (1) (1992) 136–143. doi:10.2514/3.23453.
URL https://doi.org/10.2514/3.23453

[24] A. Dumas, C. Castan, Aerodynamic Integration of High Speed Propeller on Aircraft Recent Investigations in European Wind Tunnels, in: 21st ICAS Congress,

Melbourne (Australia), International Council of the Aeronautical Sciences, 1998, pp. 1–11, Paper ICAS-98-5.10.3.
URL http://www.icas.org/ICAS_ARCHIVE/ICAS1998/PAPERS/5103.PDF

[25] M. Amato, F. Boyle, J. Eaton, P. Gardarein, Euler/Navier-Stokes simulation for propulsion airframe integration of advanced propeller-driven aircraft in the European Research Programs GEMINI/APIAN, in: 21st ICAS Congress, Melbourne (Australia), International Council of the Aeronautical Sciences, 1998, pp. 1–12, Paper ICAS 98-5.10.2.
URL http://www.icas.org/ICAS_ARCHIVE/ICAS1998/PAPERS/5102.PDF

[26] J. Bousquet, P. Gardarein, Improvements on computations of high speed propeller unsteady aerodynamics, Aerospace science and technology 7 (6) (2003) 465–472. doi:https://doi.org/10.1016/S1270-9638(03)00046-4.
URL http://www.sciencedirect.com/science/article/pii/S1270963803000464

[27] J. Frota, E. Maury, Analysis of APIAN high speed isolated test results - Acoustics and Aerodynamics, Air and Space Europe 3 (3) (2001) 87–92. doi:https://doi.org/10.1016/S1290-0958(01)90064-4.
URL http://www.sciencedirect.com/science/article/pii/S1290095801900644

[28] C. Polacsek, P. Spiegel, F. Boyle, J. Eaton, H. Brouwer, R. Nijboer, Noise computation of high-speed propeller-driven aircraft, in: 6th Aeroacoustics Conference and Exhibit, American Institute of Aeronautics and Astronautics, 2000, Paper AIAA-2000-2086. doi:10.2514/6.2000-2086.
URL https://doi.org/10.2514/6.2000-2086

[29] I. Samuelsson, Low speed wind tunnel investigation of propeller slipstream aerodynamic effects on different nacelle/wing combinations, in: ICAS, Congress, 16 th, Jerusalem (Israel), International Council of the Aeronautical Sciences, 1988, pp. 1749–1765, Paper ICAS-88-4.11.1.
URL http://www.icas.org/ICAS_ARCHIVE/ICAS1988/ICAS-88-4.11.1.pdf

[30] I. Samuelsson, Experimental investigation of low speed model propeller slipstream aerodynamic characteristics including flow field surveys and nacelle/wing static pressure measurements, in: ICAS, Congress, 17 th, Stockholm (Sweden), Interna-

tional Council of the Aeronautical Sciences, 1990, pp. 71–84, Paper ICAS-90-3.1.3.
URL http://www.icas.org/ICAS_ARCHIVE/ICAS1990/ICAS-90-3.1.3.pdf

[31] P. Lotsted, Propeller slip-stream model in subsonic linearized potential flow, Journal of Aircraft 29 (6) (1992) 1098–1105. doi:10.2514/3.56865.
URL https://doi.org/10.2514/3.56865

[32] P. Lotsted, A propeller slipstream model in subsonic linearized potential flow, in: ICAS, Congress, 17 th, Stockholm (Sweden), International Council of the Aeronautical Sciences, 1990, pp. 733–744, paper ICAS-90-5.4.4.
URL http://www.icas.org/ICAS_ARCHIVE/ICAS1990/ICAS-90-5.4.4.pdf

[33] A. Stuermer, Unsteady euler and navier-stokes simulations of propellers with the unstructured dlr tau-code, in: New Results in Numerical and Experimental Fluid Mechanics V, Springer, 2006, pp. 144–151. doi:10.1007/978-3-540-33287-9_18.

[34] S. Leth, F. Samuelsson, S. Meijer, Propeller Noise Generation and its Reduction on the Saab 2000 High-Speed Turboprop, in: 4th AIAA/CEAS Aeroacoustics Conference, American Institute of Aeronautics and Astronautics, 1998, pp. 457–463, Paper AIAA-98-2283. doi:10.2514/6.1998-2283.
URL https://doi.org/10.2514/6.1998-2283

[35] U. Emborg, F. Samuelsson, J. Holmgren, S. Leth, Active and passive noise control in practice on the saab 2000 high speed turboprop, in: 4th AIAA/CEAS aeroacoustics conference, American Institute of Aeronautics and Astronautics, 1998, pp. 1–5. doi:10.2514/6.1998-2231.
URL https://doi.org/10.2514/6.1998-2231

[36] F. Farassat, G. Succi, A review of propeller discrete frequency noise prediction technology with emphasis on two current methods for time domain calculations, Journal of Sound and Vibration 71 (3) (1980) 399–419. doi:https://doi.org/10.1016/0022-460X(80)90422-8.
URL http://www.sciencedirect.com/science/article/pii/0022460X80904228

[37] M. De Gennaro, D. Caridi, M. Pourkashanian, Ffowcs William-Hawkings Acoustic Analogy for Simulation of NASA SR2 Propeller Noise in Transonic Cruise Condition, in: V ECCOMAS CFD, European Conference on Computational Fluid

Dynamics, Lisbon (Portugal), 2010, pp. 1–16.
URL http://http://pubdb.ait.ac.at/files/PubDat_AIT_129832.pdf

[38] C. Tan, K. Voo, W. Siauw, J. Alderton, A. Boudjir, F. Mendonça, CFD Analysis of the Aerodynamics and Aeroacoustics of the NASA SR2 Propeller, in: ASME Turbo Expo 2014: Turbine Technical Conference and Exposition, Vol. 2A:Turbomachinery, American Society of Mechanical Engineers, 2014, pp. 1–11, Paper GT2014-26779. doi:10.1115/GT2014-26779.
URL http://dx.doi.org/10.1115/GT2014-26779

[39] B. Marinus, M. Roger, R. Van de Braembussche, Aeroacoustic and Aerodynamic Optimization of Aircraft Propeller Blades, in: 16th AIAA/CEAS Aeroacoustics Conference, American Institute of Aeronautics and Astronautics, 2010, pp. 1–17, Paper AIAA 2010-3850. doi:10.2514/6.2010-3850.
URL https://doi.org/10.2514/6.2010-3850

[40] G. Chirico, G. Barakos, N. Bown, Numerical aeroacoustic analysis of propeller designs, The Aeronautical Journal 122 (1248) (2018) 283–315. doi:10.1017/aer.2017.123.
URL https://doi.org/10.1017/aer.2017.123

[41] M. Cojocaru, M. Niculescu, M. Pricop, Aero-acoustic assessment of installed propellers, INCAS Bulletin 7 (2) (2015) 53–62. doi:10.13111/2066-8201.2015.7.2.5.
URL http://dx.doi.org/10.13111/2066-8201.2015.7.2.5

[42] R. Akkermans, M. Pott-Pollenske, H. Buchholz, J. Delfs, D. Almoneit, et al., Installation Effects of a Propeller Mounted on a High-Lift Wing with a Coanda Flap. Part I: Aeroacoustic Experiments, in: 20th AIAA/CEAS Aeroacoustics Conference - AIAA AVIATION Forum, American Institute of Aeronautics and Astronautics, 2014, pp. 1–14, Paper AIAA 2014-3191. doi:10.2514/6.2014-3191.
URL https://doi.org/10.2514/6.2014-3191

[43] C. Lenfers, N. Beck, R. Radespiel, Numerical and experimental investigation of propeller slipstream interaction with active high lift wing, in: 35th AIAA Applied Aerodynamics Conference - AIAA AVIATION Forum, American Institute

of Aeronautics and Astronautics, 2017, pp. 1–14. doi:10.2514/6.2017-3248.
URL https://arc.aiaa.org/doi/pdf/10.2514/6.2017-3248

[44] J. Yin, A. Stuermer, M. Aversano, Aerodynamic and aeroacoustic analysis of installed pusher-propeller aircraft configurations, Journal of Aircraft 49 (5) (2012) 1423–1433. doi:10.2514/1.C031704.
URL https://doi.org/10.2514/1.C031704

[45] A. Pagano, M. Barbarino, D. Casalino, L. Federico, Tonal and Broadband Noise Calculations for Aeoacoustic Optimization of a Pusher Propeller, Journal of Aircraft 47 (3) (2010) 835–848. doi:10.2514/1.45315.
URL https://doi.org/10.2514/1.45315

[46] E. Envia, Aeroacoustic Analysis of a High-Speed Open Rotor, International Journal of Aeroacoustics 14 (3-4) (2015) 569–606. doi:10.1260/1475-472X.14.3-4.569.
URL https://doi.org/10.1260/1475-472X.14.3-4.569

[47] A. Sharma, H.-N. Chen, Prediction of aerodynamic tonal noise from open rotors, Journal of Sound and Vibration 332 (16) (2013) 3832–3845. doi:https://doi.org/10.1016/j.jsv.2013.02.027.
URL http://www.sciencedirect.com/science/article/pii/S0022460X13001806

[48] C. Kendall-Torry, F. Danner, Investigations on direct and hybrid sound predictions, in: ASME Turbo Expo 2016: Turbomachinery Technical Conference and Exposition, Vol. Volume 2A: Turbomachinery, American Society of Mechanical Engineers, 2016, pp. 1–15, Paper GT2016-57612. doi:doi:10.1115/GT2016-57612.
URL http://dx.doi.org/10.1115/GT2016-57612

[49] S. Gaggero, D. Villa, S. Brizzolara, RANS and PANEL method for unsteady flow propeller analysis, Journal of Hydrodynamics, Ser. B 22 (5, Supplement 1) (2010) 564–569. doi:https://doi.org/10.1016/S1001-6058(09)60253-5.
URL http://www.sciencedirect.com/science/article/pii/S1001605809602535

[50] D. Blunt, Altitude and airspeed effects on the optimum synchrophase angles for a four-engine propeller aircraft, Journal of Sound and Vibration 333 (16) (2014)

3732–3742. doi:https://doi.org/10.1016/j.jsv.2014.03.038.
URL http://www.sciencedirect.com/science/article/pii/S0022460X14002399

[51] D. Hammond, R. McKinley, B. Hale, Noise reduction efforts for special operations c-130 aircraft using active synchrophaser control, Tech. rep., Air Force Rsearch Lab,Wright Patterson AFB,OH,45433 (1998).
URL http://www.dtic.mil/dtic/tr/fulltext/u2/a434029.pdf

[52] F. Pla, G. Goodman, Method and apparatus for synchronizing rotating machinery to reduce noise, US Patent 5221185 (June 1993).
URL https://www.google.com/patents/US5221185

[53] F. Pla, Method for reducing noise and/or vibration from multiple rotating machines, US Patent 5789678 (August 1998).
URL https://www.google.com/patents/US5789678

[54] D. Kaptein, Propeller blade position controller, US Patent 5551649, DE69526464D1, EP0663337B1 (September 1996).
URL https://www.google.com/patents/US5551649

[55] B. Magliozzi, Adaptive synchrophaser for reducing aircraft cabin noise and vibration, US Patent 5453943, WO1995022488A1 (September 1995).
URL https://patents.google.com/patent/WO1995022488A1/en

[56] L. Eriksson, Active sound attenuation system with on-line adaptive feedback cancellation, US Patent 4677677, CA1282161C (June 1987).

[57] X. Huang, L. Sheng, Y. Wang, Propeller synchrophase angle optimization of turboprop-driven aircraftan experimental investigation, Journal of Engineering for Gas Turbines and Power 136 (11) (2014) 112606–1–112606–9. doi:10.1115/1.4027644.
URL http://dx.doi.org/10.1115/1.4027644

[58] G. Barakos, C. Johnson, Acoustic comparison of propellers, International Journal of Aeroacoustics 15 (6-7) (2016) 575–594. doi:10.1177/1475472X16659214.
URL https://doi.org/10.1177/1475472X16659214

[59] F. Menter, Two-Equation Eddy-Viscosity Turbulence Models for Engineering Applications, AIAA Journal 32 (8) (1994) 1598–1605. doi:10.2514/3.12149.
URL https://doi.org/10.2514/3.12149

[60] G. Barakos, R. Steijl, K. Badcock, A. Brocklehurst, Development of CFD Capability for Full Helicopter Engineering Analysis, in: 31st European Rotorcraft Forum, Florence (Italy), 2005, pp. 1–15.

[61] R. Steijl, G. Barakos, K. Badcock, A Framework for CFD Analysis of Helicopter Rotors in Hover and Forward Flight, International Journal for Numerical Methods in Fluids 51 (8) (2006) 819–847. doi:10.1002/fld.1086.
URL http://dx.doi.org/10.1002/fld.1086

[62] S. Lawson, M. Woodgate, R. Steijl, G. Barakos, High Performance Computing for Challenging Problems in Computational Fluid Dynamics, Progress in Aerospace Sciences 52 (2012) 19–29, Applied Computational Aerodynamics and High Performance Computing in the UK. doi:https://doi.org/10.1016/j.paerosci.2012.03.004.
URL http://www.sciencedirect.com/science/article/pii/S0376042112000371

[63] S. Osher, S. Chakravarthy, Upwind Schemes and Boundary Conditions with Applications to Euler Equations in General Geometries, Journal of Computational Physics 50 (3) (1983) 447–481. doi:https://doi.org/10.1016/0021-9991(83)90106-7.
URL http://www.sciencedirect.com/science/article/pii/0021999183901067

[64] J. Boussinesq, Théorie de l'Écoulement Tourbillonant et Tumultueux des Liquides dans des Lits Rectilignes à Grande Section, Tome I-II (Theory of the swirling and turbulent flow of liquids in straight channels of large section, Volume I-II), 1st Edition, Gaulthier-Villars, Paris, France, 1897.

[65] A. Hellsten, New advanced kw turbulence model for high-lift aerodynamics, AIAA journal 43 (9) (2005) 1857–1869. doi:10.2514/1.13754.
URL https://doi.org/10.2514/1.13754

[66] B. van Leer, Flux-vector Splitting for the Euler Equations, in: Eighth International Conference on Numerical Methods in Fluid Dynamics, Springer Berlin Heidelberg, 1997, pp. 507–512. doi:10.1007/978-3-642-60543-7_5.

[67] G. van Albada, B. van Leer, W. Roberts Jr, A Comparative Study of Computational Methods in Cosmic Gas Dynamics, in: Upwind and High-Resolution Schemes, Vol. 2, Springer Berlin Heidelberg, 1997, pp. 95–103. doi:10.1007/978-3-642-60543-7_6.
URL https://doi.org/10.1007/978-3-642-60543-7_6

[68] O. Axelsson, Iterative Solution Methods, Cambridge University Press, Cambridge, MA, 1994. doi:10.1017/CBO9780511624100.
URL https://doi.org/10.1017/CBO9780511624100

[69] N. Scrase, M. Maina, The evaluation of propeller aero-acoustic design methods by means of scaled-model testing employing pressure tapped blades and spinner, in: ICAS PROCEEDINGS, International Council of the Aeronautical Sciences, 1994, pp. 183–195, Paper ICAS-94-6.1.2.

[70] A. Gomariz-Sancha, M. Maina, A. J. Peace, Analysis of Propeller-Airframe Interaction Effects through a Combined Numerical Simulation and Wind-Tunnel Testing Approach, in: AIAA SciTech Forum, 53rd AIAA Aerospace Sciences Meeting, Kissimmee, Florida, 2015, pp. 1–19, Paper AIAA 2015-1026. doi:10.2514/6.2015-1026.
URL https://doi.org/10.2514/6.2015-1026

[71] A. Knepper, N. Bown, IMPACTA Wind-Tunnel Instrumentation Specification, Tech. Rep. ITS 01777, Issue 3, Dowty Propellers (GE Aviation Systems Ltd) (2014).

[72] R. Steijl, G. Barakos, Sliding Mesh Algorithm for CFD Analysis of Helicopter RotorFuselage Aerodynamics, International Journal for Numerical Methods in Fluids 58 (5) (2008) 527–549. doi:10.1002/fld.1757.
URL http://dx.doi.org/10.1002/fld.1757

[73] M. Jarwowsky, M. Woodgate, G. Barakos, J. Rokicki, Towards Consistent Hybrid Overset Mesh Methods for Rotorcraft CFD, International Journal for Numerical Methods in Fluids 74 (8) (2014) 543–576. doi:10.1002/fld.3861.
URL http://dx.doi.org/10.1002/fld.3861

[74] E. Geurts, IMPACTA Transmission functions generation - test and processing., Tech. Rep. NLR-CR-2013-145, National Aerospace Laboratory NLR (2013).

[75] Dowty Aerospace Propellers, (Accessed 23 February 2018).
URL http://dowty.com